buildings

MDPI

Article

Modelling of FRP-Strengthened Masonry Buildings with Equivalent Frame Models

Ivana Božulić [1,*], Francesco Vanin [2] and Katrin Beyer [1]

[1] Earthquake Engineering and Structural Dynamics Laboratory (EESD), School of Architecture, Civil and Environmental Engineering (ENAC), École Polytechnique Fédérale de Lausanne (EPFL), 1015 Lausanne, Switzerland; katrin.beyer@epfl.ch

[2] Résonance Ingénieurs-Conseils SA, 1227 Carouge, Switzerland; francesco.vanin@resonance.ch

* Correspondence: ivana.bozulic@gmail.com

Abstract

Existing masonry buildings can be strengthened to reduce their seismic vulnerability. While the effect of strengthening on the structural elements of a building has been well researched, there are few computationally efficient numerical modelling approaches that capture the effect of strengthening interventions. This paper shows how a recently developed macro-element for unreinforced masonry walls, which can capture both in-plane and out-of-plane failure modes, can model the effect of fibre-reinforced polymer (FRP) strengthening on masonry walls. Practically, FRP strengthening increases the flexural in-plane and out-of-plane strength through longitudinal FRP strips placed against the masonry. In the macro-element, this is modelled through adding fibres to the section model that represent the longitudinal FRP strips. Transversal FRP strips affect the shear strength and in the macro-element this is accounted for by increasing the cohesion in the equation for the shear strength of the macro-element. This paper models quasi-static and dynamic in-plane shear–compression tests as well as out-of-plane bending tests on walls with and without FRP strengthening and compares the numerical simulations to experimental results taken from the literature. The proposed modelling approach for FRP-strengthened masonry walls accurately predicts their in-plane and out-of-plane response, indicating that equivalent frame models can be used to predict the response of masonry buildings with FRP-strengthened walls. The application of the approach is illustrated through hypothetical retrofit configurations of a masonry building that was tested on a shake table in its unstrengthened state.

Keywords: fibre-reinforced polymer; equivalent frame models; in-plane capacity; shear reinforcement; stone masonry; building strengthening

Check for updates

Academic Editor: Gabriele Milani

Received: 28 July 2026
Revised: 19 October 2026
Accepted: 24 October 2026
Published: 30 October 2026

Copyright: © 2026 by the authors. Licensee MDPI, Basel, Switzerland. This article is an open access article distributed under the terms and conditions of the Creative Commons Attribution (CC BY) license.

1. Introduction

In Europe, many residential buildings and the majority of heritage buildings are unreinforced masonry (URM) structures. Recent earthquakes such as the ones in Central Italy (2009, 2016) and Croatia (2020) confirmed again the high seismic vulnerability of these structures [1–4]. To improve the performance of URM structures in an earthquake, retrofitting measures can be undertaken, though it is often difficult to predict how these measures will react in an actual seismic event. To assess their performance and plan retrofit interventions, the engineering community needs reliable tools for predicting the seismic behaviour of URM buildings in their unstrengthened and, where applicable, strengthened configuration.

Due to its limited tensile strength, the response of URM is nonlinear even for small deformation demands [5]; therefore, nonlinear analysis methods that capture all rele-

vant failure modes of URM elements are required to describe its response to seismic activity [6–8]. D'Altri et al. [9] provide a comprehensive overview of existing numerical modelling approaches. Because they offer a good compromise between accuracy and numerical efficiency, equivalent frame models (EFMs) are widely used for modelling the nonlinear seismic response of entire masonry buildings [10–13]. In these models, the masonry façade is idealised as a frame of macroscopic wall elements that are nonlinear and connected by rigid links representing the portions of masonry typically undergoing only small deformations [10]. Existing formulations of EFM macro-elements model only the in-plane behaviour of masonry elements [10,11,14,15], requiring additional analyses to assess the out-of-plane response of the masonry walls. A recently developed macro-element by Vanin et al. [13] captures both the in-plane and out-of-plane response of the single element. This approach has been used successfully to model unstrengthened URM buildings that were tested on shake tables [16].

Retrofitting interventions are designed to reduce the seismic vulnerability of the building response, and numerous retrofitting techniques have been developed for repairing and strengthening masonry structures, ranging from composite materials to steel-based systems such as steel grids and steel web plates [17]; for a recent review, see [18,19]. Among these, retrofitting with composite polymer materials, particularly fibre-reinforced polymers (FRPs) are the most widely used. In order to carry the additional tensile stresses, FRPs are bonded to the exterior surface of the structural member in the appropriate position. FRP presents a convenient solution because of its favourable strength-to-mass ratio, resistance to corrosion and simple application [20]. However, retrofitting with FRP has also several disadvantages, such as low resistance to extreme temperatures [21], impermeability, non-removability and early debonding from weak substrate [22].

Strengthening one element can lead to the failure of another, making it important to evaluate the full system response through numerical modelling of the entire building. In the literature, there are examples of other structural systems with different retrofit configurations being assessed under the same seismic input, such as the comparison of different steel plate shear walls under near-field ground motions [23] and of steel plate shear walls with different slot configurations [24,25], the response control of mega-subcontrolled structural systems [26] and the performance of mega column-core tube-outrigger structures [27]. Incremental dynamic analysis has also been used to identify the failure modes of such systems and to optimise their configuration [28]. For URM buildings, such comparisons require a model that is efficient enough for many nonlinear dynamic analyses and that captures the relevant failure modes of both unstrengthened and strengthened walls. Therefore, the objective of this paper is to develop and validate an approach for modelling FRP-strengthened URM buildings with EFMs. We herein show that the novel macro-element developed originally by Vanin et al. [13], which captures the in-plane and out-of-plane response of a masonry panel simultaneously, can be used to examine the effects of FRP strengthening (both flexural and shear) on the in-plane and out-of-plane capacity of masonry walls and on the global behaviour of a building. By combining these capabilities within an equivalent frame model, our approach enables the dynamic seismic assessment of the full system response of FRP-retrofitted URM buildings, including the interaction between in-plane and out-of-plane failure modes across multiple walls and storeys.

In Section 2, we review the experimental campaigns on FRP-strengthened masonry panels that have been tested in the laboratory. From these, we chose campaigns that investigate the in-plane and out-of-plane response of FRP-strengthened masonry walls under static and dynamic loading. We also review, in Section 2, the literature on modelling FRP-strengthened URM walls and on strength models for FRP-strengthened URM walls. In

Section 3, we present our modelling strategy for FRP-strengthened masonry walls subjected to in-plane and out-of-plane loading, which relies on the macro-element by Vanin et al. [13]. Using this macro-element, we model the in-plane and out-of-plane flexural capacity using fibre sections with corresponding uni-axial material laws for masonry and FRP. We model the increase in in-plane shear strength due to FRP strengthening through an increase in the cohesion part of the Mohr–Coulomb law that represents the shear strength. In Section 4, we then validate this modelling approach by applying it to the selected test campaigns and compare the obtained numerical response to the experimental one. We determine that this approach represents well the response of the retrofitted masonry panels. Finally, in Section 5, we demonstrate the usefulness of our approach by applying it to the model of an entire building and show how various retrofitting solutions influence the full system response. For this purpose, we chose a URM building that has been tested in its unstrengthened configuration on a shake table [29] and simulate the effect of hypothetical FRP-strengthening interventions. In Section 6, we discuss the applicability and limitations of the approach with respect to masonry types and strengthening schemes. All files for computing the macro-element properties as well as the input and results files of the analyses are shared openly through the Zenodo repository https://doi.org/10.5281/zenodo.4733243. This is further described in Data Availability Statement.

2. Literature Review

In this section, we review the literature on in-plane and out-of-plane tests that have been conducted on FRP-strengthened URM walls, modelling FRP-strengthened URM panels and strength models for FRP-strengthened URM walls. We used this literature review to choose appropriate experimental campaigns for the validation of the later-developed modelling approach.

2.1. Experimental Tests on FRP-Strengthened URM Walls

In this section, we briefly summarise in-plane shear compression tests and out-of-plane tests on FRP-strengthened URM walls. Simple compression and diagonal compression tests are not reviewed.

Many researchers have investigated the effect of FRP-strengthening on the in-plane strength of URM walls through shear–compression tests. Triantafillou [30] tested four wallets strengthened with horizontal carbon FRP (CFRP) laminates. Chuang et al. [31] investigated the effect of CFRP strips along the edges and tested walls with and without such strips. ElGawady et al. [32] tested brick masonry walls that were strengthened on one side with glass or aramid FRP. Next to quasi-static cyclic tests, ElGawady et al. [33] also carried out shake table tests on such walls. Stratford et al. [34] tested clay brick masonry walls reinforced with either glass FRP (GFRP) strips arranged as a truss or GFRP sheets. Wang et al. [35] investigated the efficiency of GFRP plies in three configurations (only horizontal strips; primary and secondary diagonals; three horizontal strips together with primary diagonals). Marcari et al. [36] carried out monotonic tests on tuff masonry walls strengthened on both sides with carbon or glass FRP strips. Alcaino and Santa-Maria [37] investigated sixteen hollow clay brick masonry walls strengthened with horizontal or diagonal CFRP strips. Capozucca [38] tested walls with vertical, horizontal and diagonal GFRP strips organized as a truss. Zhou et al. [39] tested walls strengthened with basalt FRP configured into diagonal and horizontal strips. Triller et al. [40] presented an overview of testing campaigns performed both in situ and in the laboratory. Brick walls were strengthened using carbon and glass fibres applied in various layouts.

Campaigns on the out-of-plane behaviour of FRP-strengthened brick masonry walls investigated the influence of the testing procedure and the reinforcement type and layout

on the out-of-plane strength. For instance, carbon FRP was used for strengthening by Triantafillou [30], Hamed and Rabinovitch [41] and Anil et al. [42], who tested masonry elements as simply supported beams subjected to monotonically increased point forces. Willis et al. [43] used a cyclic loading protocol to test full-scale walls with openings, first unstrengthened and then retrofitted with vertical CFRP or GFRP strips after the onset of damage. In 2004, Tan and Patoary [44] performed an extensive experimental campaign consisting of thirty solid clay brick walls strengthened with GFRP, CFRP or fibreglass-woven roving reinforcement. The walls were simply supported along the four sides and subjected to monotonic point and distributed loads. Mosallam [45] tested full-scale red brick walls strengthened along the entire wall face with GFRP or CFRP under a hydraulic pressure load. Sistani Nezhad and Kabir [46] tested traditional Iranian masonry walls strengthened with GFRP under monotonic loading. Gilstrap and Dolan [47] investigated the out-of-plane capacity of clay perforated bricks retrofitted with one or two layers of aramid and carbon polymers. Hamoush et al. [48] tested hollow clay masonry walls strengthened either by two layers of a continuous glass fibre web or by a layer of woven fabrics in one direction and a layer of aramid fibres in the other direction for the purpose of stabilization.

For the in-plane response, we validated the approach against the test campaigns by Marcari et al. [36] and ElGawady et al. [32]. We chose the tests by Marcari et al. [36] because they comprised a large range of FRP-strengthening configurations. These tests were monotonic and we complemented them by the quasi-static cyclic and the shake table tests by ElGawady et al. [32,33], whose experimental data is available in electronic format. For the out-of-plane tests, we chose the test campaign by Triantafillou [30] because the four-point tests conducted here are suitable for modelling with the macro-element, which can only capture one-way bending. In addition, Triantafillou [30] investigated two different reinforcement ratios by applying two or four carbon strips.

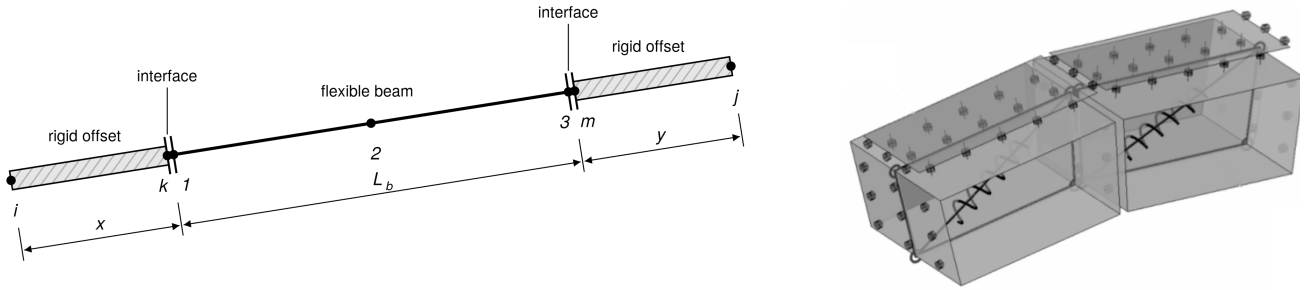
2.2. Modelling Masonry Elements Strengthened by FRP

Several strategies have been proposed to model individual masonry panels strengthened by fibre polymer systems (for instance, [49–51]). Because there is a detailed review of this topic by Wang et al. [18], we will herein discuss only the two previous studies modelling FRP-strengthened masonry walls with beam elements or macro-elements suitable for EFMs.

For the first of these studies, Grande et al. [52] modelled monotonic tests of FRP-strengthened isolated walls and an entire façade. To do this, they developed a nonlinear beam element with two rigid offsets and a flexible part consisting of a displacement-based nonlinear beam element with fibre sections (Figure 1). To model the shear failure of the masonry, Grande et al. [52] used rigid interfaces, located at either end of the flexible part of the beam element, with a limited shear strength that follows a Mohr–Coulomb law. The flexural section behaviour is described through a fibre section. FRP reinforcement is described through a nonlinear material law that hypothesizes a limited strength in tension and zero strength in compression. The connection between the masonry and the FRP reinforcement is assumed to be perfect, with possible debonding accounted for through the value of the ultimate FRP strain. However, because the beam element by Grande et al. [52] can only capture in-plane deformations, the effect of FRP-strengthening on the out-of-plane strength of the masonry walls cannot be considered. Furthermore, Grande et al. [52] state that the effect of FRP strengthening on the shear strength could be considered by increasing the shear strength, but in the case studies, they assume that FRP-strengthening suppresses shear failure modes.

A similar approach was applied by Salvatori et al. [53] to masonry piers strengthened with timber frames and OSB panels, using a three-dimensional macro-element in which the strengthening is represented by additional fibres and its shear contribution by calibrated increases in cohesion and friction. That approach has so far been validated only for in-plane quasi-static loading.

To enhance the macro-element proposed by Caliò et al. [54] to model FRP-strengthened masonry arches, Pantò et al. [55] added the FRP elements as zero-thickness rigid plates and sets of nonlinear springs that are elasto-brittle in tension and have zero compressive strength (Figure 1). Debonding and delamination was modelled by nonlinear axial and shear springs, respectively, between panels and FRP plates.



(**a**) (**b**)

Figure 1. (**a**) The schematic of the beam element proposed by Grande et al. [52]; (**b**) Representation of FRP-reinforced macro-element in Pantò et al. [55]. (CC BY 4.0)

In summary, previous research on modelling FRP-strengthened masonry with macro-elements was carried out by Grande et al. [52] and Pantò et al. [55]. Ref. [52] considered the effect of FRP strengthening on the in-plane response of walls, while [55], extending the macro-element of Caliò et al. [54], modelled curved masonry structures such as arches. Since a newly developed macro-element by Vanin et al. [13] enables an integrated in-plane and out-of-plane assessment of a masonry construction, we use it here to assess the effect of FRP-strengthening on the in-plane and out-of-plane response simultaneously. For the flexural response we follow the approach by Grande et al. [52] and represent the FRP reinforcement through additional fibres in the fibre section. For the shear response, we modify the cohesion part of the Mohr–Coulomb law, which describes the shear capacity of the macro-element by Vanin et al. [13]. To do so, we review in the next section engineering models for computing the shear strength increase in masonry panels due to FRP strengthening. The adopted modelling strategy, both for the flexural and shear response, is described in detail in Section 3.

2.3. Engineering Models for the Shear Strength of FRP-Strengthened URM Panels

Though there are several models for the in-plane shear strength of FRP-strengthened URM walls, similar models do not exist for the in-plane and out-of-plane flexural strength and the out-of-plane shear strength. The latter is typically not critical for masonry walls since the shear force at out-of-plane flexural failure is a small fraction of the axial load [56]. Accordingly, the out-of-plane shear response of the macro-element is linear elastic [13], and we do not model an increase in out-of-plane shear strength due to FRP strengthening. The increase in in-plane and out-of-plane flexural strength, on the other hand, can be computed as discussed in Section 3.

Several guidelines and design standards propose strength models that address the in-plane shear strength of masonry panels with externally bonded FRPs; a review of these models can be found in Zhuge [20] and Stepinac et al. [57]. All models calculate the shear

strength of the masonry panel with externally bonded FRPs as the sum of the shear strength of the uncracked masonry panel plus the shear strength resulting from the FRP shear reinforcement.

$$V = V_m + V_{FRP}. \tag{1}$$

The additional capacity provided by FRP reinforcement depends on several factors: the layout of the FRP strips, the mechanical properties of the composite, the orientation of fibres, the anchorage length and the reached strain [20]. The failure of FRP strips can occur either due to debonding of the strip from the masonry or the rupture of the fibres [58]. The developed failure mechanism depends on the bond between the substrate and composite [59], the anchorage length, presence of connectors at the FRP ends, the thickness of the laminate, etc. In most cases, local debonding occurs before the FRPs reach their maximum tensile strength.

Regarding the FRP strain at failure, strength models differ in terms of the reinforcement layout and assumptions. Triantafillou [30] proposed the first model for the shear strength of FRP-strengthened masonry panels. This model uses a truss analogy that assumes that only the laminates orthogonal to the element axis contribute to the shear strength. Any effect of the laminates parallel to the element axis is neglected, and diagonal layouts were not considered. According to Triantafillou [30], the contribution of the FRP laminates to the shear resistance of the masonry wall can be computed as:

$$V_{FRP} = \rho_h \cdot t \cdot L \cdot E_{FRP} \cdot \varepsilon_{FRP}, \tag{2}$$

where ρ_h is the FRP reinforcement ratio in the horizontal direction, t and L are the thickness and the length of the wall, respectively, E_{FRP} is the Young's modulus of the FRP and ε_{FRP} is the maximum effective strain of the FRP. The latter parameter was calibrated against experimental test data wherein fibre rupture occurred. Triantafillou and Antonopoulos [60] refined this model by proposing new expressions for predicting the effective maximum strain. These expressions were also obtained from the regression of experimental data, which included different failure mechanisms (i.e., rupture of fibres, debonding in the middle or at the end of the strip) and composite materials (carbon FRP and aramid FRP).

Models for computing the shear resistance of FRP-strengthened masonry walls are also included in the Italian guidelines Consiglio Nazionale delle Ricerche [58] and the American standard ACI-440.7R-10 [61], while the European EN 1998-1:2004 [62] does not provide any shear strength equations for FRP-strengthened URM walls. Both guidelines adopt the truss model proposed by Triantafillou [30] and differ only in terms of the truss geometry and the effective FRP strain at failure. The Italian guidelines Consiglio Nazionale delle Ricerche [58] write the shear strength of FRP-strengthened masonry walls (partial safety factors are omitted) as:

$$V_{FRP} = \frac{0.6 d_{wall} \cdot A_{FRP} \cdot E_{FRP} \cdot \varepsilon_{FRP}}{p_{FRP}}, \tag{3}$$

where ε_{FRP} is the maximum strain allowed in the FRP (minimum value between the strain at rupture or debonding of the FRP), d_{wall} is the distance between the compression side of the wall and the centroid of the FRP flexural strengthening, E_{FRP} is the FRP Young's modulus of elasticity, A_{FRP} is the area of the FRP strips running parallel to the element axis, and p_{FRP} is the centre-to-centre spacing of FRP strips measured orthogonally to the fibre direction. This equation is equal to Equation (2), differing only in that the wall length L is replaced by $0.6 d_{wall}$. Since it accounts for strips orthogonal to the element axis, this formula is used in our computations, for walls with a grid layout of FRP in the following.

For diagonal layouts, Equation (6) is applied instead. A value of the FRP strain at failure is usually provided in the specification of the composite, while Consiglio Nazionale delle Ricerche [58] estimates the mean strain corresponding to end debonding as:

$$\varepsilon_{fd,end} = \sqrt{\frac{2\Gamma_{Fm}}{E_{FRP}t_{FRP}}}, \tag{4}$$

where t_{FRP} is the thickness of the reinforcement, E_{FRP} is the FRP Young's modulus of elasticity and Γ_{Fm} is the mean specific fracture energy of the masonry strengthened by FRP. This parameter can be computed as Equation (5) [58]:

$$\Gamma_{Fm} = c_1\sqrt{f_{mm}f_{mtm}}, \tag{5}$$

where f_{mm} is the mean compressive strength of masonry, f_{mtm} is the mean tensile strength of masonry and c_1 is an empirically determined coefficient that depends on the geometry and type of masonry. Since c_1 significantly influences the specific fracture energy of FRP-strengthened masonry and, therefore, also the end debonding strain and the maximum shear force [63], the proposed value of c_1 should be calibrated more accurately in the future, as it was so far determined from only a limited number of experiments. Furthermore, the CNR provides values only for perforated bricks, tuff bricks and calcarenite or Lecce stone. The debonding along the interface of masonry and laminate can occur at the end of the strip or as intermediate crack-induced debonding [63]. In absence of more accurate data, the intermediate debonding should be calculated by multiplying the value of the end debonding strain with k_{cr}, for which Consiglio Nazionale delle Ricerche [58] suggests a value of 3 that was obtained experimentally for the debonding of FRP strips from RC members.

Neither the Italian nor the American standard provides shear strength equations for masonry walls with diagonal FRP reinforcement. For this reason, Prota et al. [63] proposed the following equation:

$$V_{FRP} = A_{d,FRP} \cdot cos\alpha \cdot E_{FRP} \cdot \varepsilon_{FRP}, \tag{6}$$

where $A_{d,FRP}$ is the cross-sectional area of the diagonal strip and α is the angle of the diagonal strip with regard to the horizontal direction. Prota et al. [63] determine the maximum effective strain ε_{FRP} according to the procedure in Consiglio Nazionale delle Ricerche [58]. We will use Equations (1)–(6) for calculating the shear resistance of the FRP-strengthened walls that we simulate in Sections 4 and 5. Table 1 summarises the recommended code equations as a function of the applied FRP layout.

Table 1. Summary of approaches that compute the shear strength contribution V_{FRP} as a function of the FRP layout.

FRP Layout	Approach by	Equation (s)
Strips only orthogonal to the beam axis	Triantafillou [30]	(2)
Diagonal strips	Prota et al. [63]	(6)
Combination of strips parallel and orthogonal to the beam axis	CNR	(3)
End debonding of FRP	CNR	Equation (4)
Intermediate debonding of FRP	CNR	Equation (4) × k_{cr}

3. Modelling FRP-Strengthened URM Walls in Equivalent Frame Models

We herein develop an EFM-based modelling approach for FRP-strengthened URM walls. This modelling approach is validated in Section 4 against laboratory tests on FRP-strengthened walls. We base our EFM model of masonry walls on the three-dimensional macro-element by Vanin et al. [13], which has been implemented in OpenSEES [64]. Building on the in-plane response of the macro-element by Penna et al. [11], this newer macro-element has been augmented to also reproduce the out-of-plane dynamic response of masonry panels, as shown in Figure 2. For this purpose, the flexural response is not only captured by nonlinear sections at the element ends as in Penna et al. [11] but by an additional nonlinear section at midlength of the element. All three sections account for nonlinear deformations due to axial strains, capturing therefore the interaction between axial response and in-plane and out-of-plane flexural response. Unlike in Penna et al. [11], the in-plane flexural capacity can not only be defined by analytical integration of stresses but also via fibre sections, an option that we will use for modelling the effect of strengthening. More specifically, three different fibre sections can be defined for the three nonlinear sections at the element ends and at midlength; we will use this option to represent diagonal FRP layouts and FRP-strips that are not anchored in the slabs but only glued onto the wall. In the following, we outline how we capture the increase in flexural stiffness and strength and in-plane shear strength due to FRP strengthening. Because suitable models are missing, we assume that FRP strengthening affects neither the in-plane shear stiffness nor the drift capacity of the wall. The drift capacities associated with shear and flexural failure of the macro-element by Vanin et al. [13] are therefore taken equal to those of the unstrengthened wall. This assumption does not affect the strength of the strengthened wall, which is computed from the fibre sections and the modified Mohr–Coulomb criterion, nor the governing failure mechanism. It affects only the drift at which the strength drops. Keeping the drift capacity of the unstrengthened wall is conservative when the strengthening increases the deformation capacity, but it may be unconservative when FRP debonding or rupture causes a sudden loss of strength.

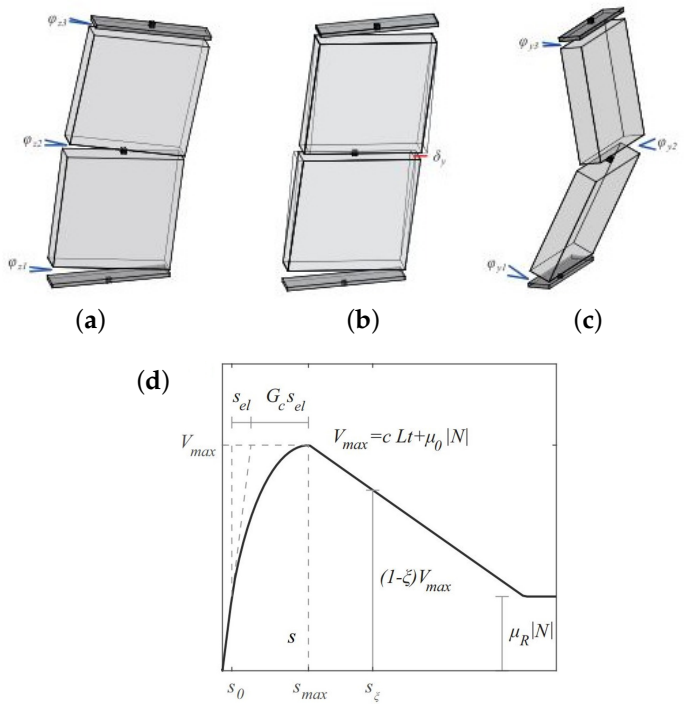


Figure 2. Vanin et al. [13]: Deformation modes of the macro-element, showing (**a**) in-plane flexure, (**b**) in-plane flexure and shear and (**c**) out-of-plane; (**d**) definition of shear response. Reproduced from

Vanin, F.; Penna, A.; Beyer, K. A three-dimensional macroelement for modelling the in-plane and out-of-plane response of masonry walls. Earthquake Engineering & Structural Dynamics 2020, 49, 1365–1387 [13]. © 2020 John Wiley & Sons, Ltd. Reprinted with permission.

All the analyses producing the results presented in this paper have been performed using OpenSEES [64].

3.1. Modelling the Flexural Stiffness and Strength of FRP-Strengthened URM Walls

The flexural properties of the macro-element by Vanin et al. [16] can be defined via fibre sections, where each fibre is assigned a cross-sectional area and a uni-axial material law (Figure 3). Therefore, we modelled the increase in flexural strength due to the FRP reinforcement by adding FRPs to the section, following the approach by Grande et al. [52]. While Grande et al. [52] assessed only the in-plane behaviour, we use here the fibre sections to capture the effect of the FRP-strengthening on the in-plane and out-of-plane flexural response. When FRPs are anchored in the slabs, all three macro-element sections are represented as fibre sections containing both masonry and FRPs. In the absence of this anchorage, only the middle section of the macro-element is reinforced. Upper and bottom sections include only masonry fibres.

First, the masonry section is represented by fibres that discretise the section along the length and through the width. Material model assigned to masonry part has zero tensile strength, limited compressive strength, a damage behaviour in compression and no strength degradation. Additional fibres are assigned the area and material properties of the FRP strips that run parallel to the element axis. For diagonal strips, the area projected onto the cross-section is considered. Strips that are orthogonal to the element axis are assumed to have no effect on the flexural strength. The modified fibre section also captures the increase in out-of-plane flexural strength due to FRP reinforcement (Figure 3). Note that adding FRP reinforcement to the fibre section also modifies the flexural stiffness of the macro-element though this effect is rarely significant for the wall response.

The macro-element formulation builds on the assumption that plane sections remain plane; therefore, debonding and delamination cannot be modelled explicitly. Instead, following the approach by Grande et al. [52], we define the maximum effective strain of the FRP reinforcement in tension such that it accounts for debonding and delamination failure. These limit strains are computed using Equation (4). If end debonding was prevented by mechanical devices or FRP wrapping, we assumed that intermediate debonding would take place. In this case, the limit strain obtained from Equation (4) was multiplied by k_{cr} (see Section 2.3). As in many previous works on modelling of FRP-strengthened masonry walls (see Section 2.2), the FRP reinforcement was modelled as linear-elastic in tension up to failure and with a compressive strength of zero. Resins used as a matrix in which the fibres were embedded were not explicitly modelled; however, the material model for FRP is built by taking into account composite material properties. Progressive degradation of the bond between FRP and masonry under cyclic loading or environmental exposure is not accounted for since the FRP material law is linear elastic up to the limit strain. For walls without end anchorage or subjected to many load cycles, the FRP contribution may therefore be overestimated. Fibres representing the masonry cross-section were assigned the material law “compression damage 1D” [16], which has no tensile strength.

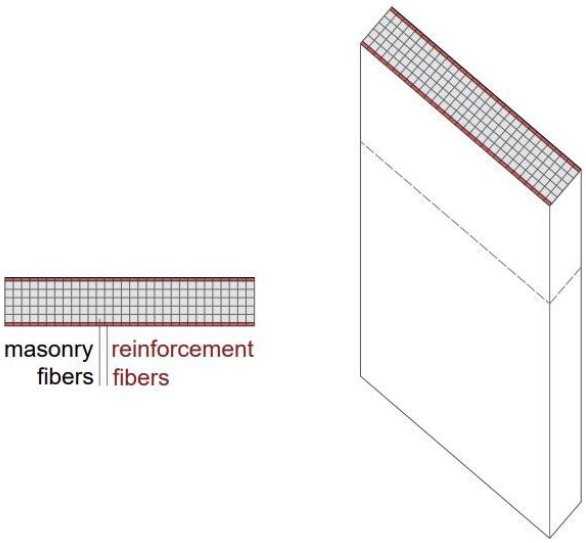


Figure 3. Fibre section of an FRP-strengthened URM wall.

3.2. Modelling the In-Plane Shear Strength of FRP-Strengthened URM Walls

In the macro-element by Vanin et al. [13], the in-plane forces are applied as nodal forces at the two end nodes, making the in-plane shear deformations constant along the element axis. The force capacity is defined by a Mohr–Coulomb criterion that couples axial and shear force [11,13] (Figure 2):

$$V_{max} = cLt + \mu_0 N. \tag{7}$$

The macro-element by Vanin et al. [13] also allows for a reduction in the friction contribution such that both an initial friction coefficient μ_0 as well as a residual friction coefficient μ_R are defined. The residual shear strength is:

$$V_{res} = \mu_R N. \tag{8}$$

After the residual strength is attained, the strength does not reduce further. The residual friction coefficient μ_R also regulates the amount of dissipated energy by controlling the shape of the hysteresis curve [13].

We assume that the FRP-strengthening does not change the shear stiffness of the masonry element, influencing only its shear strength. Since the engineering models for the shear strength of FRP-strengthened masonry treat the FRP contribution as independent of the axial load (Equation 1), it can be modelled through an increase in the cohesive contribution. The interaction between axial and shear force therefore remains that of the unstrengthened masonry, through the friction term $\mu_0 N$, and the relative contribution of the FRP decreases as the axial load increases. A possible dependence of the effective FRP strain on the axial stress is not included in these models.

We computed the increase in cohesion due to FRP strengthening from Equations 2, 3 or 6 and added this contribution to the initial cohesion of the unstrengthened wall (Equation 10). The maximum shear strength of an FRP-strengthened URM wall, given in Equation 1, can therefore be rewritten as:

$$V_{max} = (c + c_{FRP})Lt + \mu_0 N, \tag{9}$$

where

$$c_{FRP} = \frac{V_{FRP}}{A_{wall}}. \tag{10}$$

3.3. Calibration of the Material Parameters of an Unstrengthened URM Wall

To validate the proposed modelling strategy for FRP-strengthened URM walls, we calibrated all material parameters of the macro-element to match the force–displacement response of unstrengthened reference specimens. These parameters are the elastic modulus E of the masonry, the compressive strength f_c of the masonry, c, μ_0, μ_R and the drift at 20% force drop. The parameters were obtained using the automated calibration module of the SAMUEL software v1.0 [13], into which we input the geometry, axial load and digitised experimental force–displacement response of the unstrengthened reference specimen of each campaign being modelled. The module then fits the macro-element parameters so that the numerical response reproduces the measured one. The module assumes a shear modulus $G = 0.25E$, based on recent work by Wilding et al. [65]. The E-modulus and the compressive strength obtained from fitting the force–displacement hysteresis were cross-checked with the material properties reported in the test campaigns. Furthermore, it was verified that the chosen values corresponded to those presented in Kržan et al. [66]. Table 2 summarises the origin of all modelling parameters used in the simulations, both for the unstrengthened masonry and for the FRP strengthening.

Table 2. Origin of the modelling parameters.

Parameter	Origin	Source/Remarks
Geometry, axial load, boundary conditions	Measured	Test reports [30,33,36,67]
Masonry E-modulus E	Calibrated	Unstrengthened specimens
Masonry compressive strength f_c	Calibrated	Unstrengthened specimens
Shear modulus G	Literature	$G = 0.25E$ [65]
Cohesion c	Calibrated	Unstrengthened specimens
μ_0, μ_R, G_c, δ_u	Calibrated	Unstrengthened specimens
FRP E-modulus, ply thickness, rupture strain	Measured	Test reports and manufacturer data
Coefficient c_1	Code	CNR-DT 200 R1 [58]
Coefficient k_{cr}	Code	CNR-DT 200 R1 [58], $k_{cr} = 3$
Effective FRP strain ε_{FRP}	Code-derived	Equation 4, multiplied by k_{cr} where end debonding is prevented
Additional cohesion c_{FRP}	Code-derived	Equations 2, 3, 6 and 10

4. Validation Against Experimental Campaigns

The herein developed approach was validated against four experimental campaigns on FRP-strengthened URM walls that were identified in Section 2.1: (i) quasi-static monotonic in-plane tests by Marcari et al. [36], (ii) quasi-static cyclic in-plane tests by ElGawady et al. [32], (iii) dynamic cyclic in-plane tests by ElGawady et al. [32,33] and (iv) four-point out-of-plane bending tests by Triantafillou [30]. In the following sections, we describe the models that we set up for each experimental campaign. Because our goal is to validate the modelling approach for the FRP-strengthening, we first model the unstrengthened reference specimens of each campaign. We use these simulations to calibrate the masonry material parameters of the macro-element. We then use these masonry material parameters and the FRP-modelling approach described in Section 3 to model the FRP-strengthened walls. We validate the FRP-modelling approach by comparing the simulation results of the strengthened walls to the experimental results.

4.1. Monotonic In-Plane Tests

Marcari et al. [36] performed an experimental campaign on FRP-strengthened tuff masonry walls subjected to monotonic in-plane loading. Four control specimens were kept without reinforcement, while other specimens were reinforced with either a grid layout (four with CFRP and four with GFRP strips) or with a cross layout (four with CFRP and three with GFRP strips), with the reinforcement applied to both faces of the panels. The fibre density (strips applied in either one or two ply thickness) was also varied. A detailed description of the specimens is presented in Appendix A. Geometry and boundary

conditions are shown in Figure 4. The compression strength of the masonry in this testing campaign was equal to 1.4 MPa.

The macro-element input parameters were fitted for all four reference panels without reinforcement following the approach outlined in Section 3.3. Table 3 summarises the obtained material values for the four reference panels. Since the experimental results varied significantly, simulations of the wall panels were carried out using three sets of parameters corresponding to the mean, minimum and maximum values of the mechanical properties. The obtained mean value of the E-modulus of the masonry was 340 MPa, which is considerably lower than the 630 MPa from simple compression tests reported by Marcari et al. [68]. They computed the E-modulus as a secant modulus between 10 and 40% of the compressive strength. Regardless, significant differences in E-moduli derived from simple compression tests versus back-calculated from horizontal load tests are not uncommon for masonry walls; very similar observations are reported by Vanin et al. [69] for stone masonry walls. Finally, the comparison between the experimental data and the numerically obtained curves of unreinforced walls is shown in Figure 5. All reference specimens showed a shear failure.

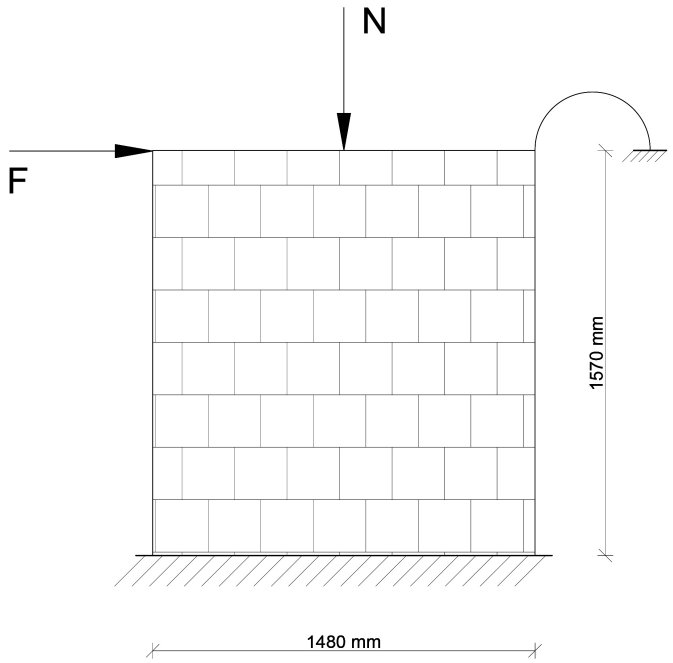


Figure 4. Boundary conditions of the walls tested by Marcari et al. [36]. Note that rotations are restrained at the top of the wall.

Table 3. Resulting output from our model for the simulation of the tests carried out by Marcari et al. [36]: Calibrated parameters for four reference specimens.

Specimen	f_c [MPa]	E [MPa]	G [MPa]	μ_0	μ_R	G_c	c [MPa]	δ_u [%]
Min	1.66	320	80	0.20	0.10	1.42	0.017	0.76
Max	1.66	370	90	0.38	0.19	1.72	0.032	1.28
Mean	1.66	340	80	0.28	0.14	1.34	0.024	1.027

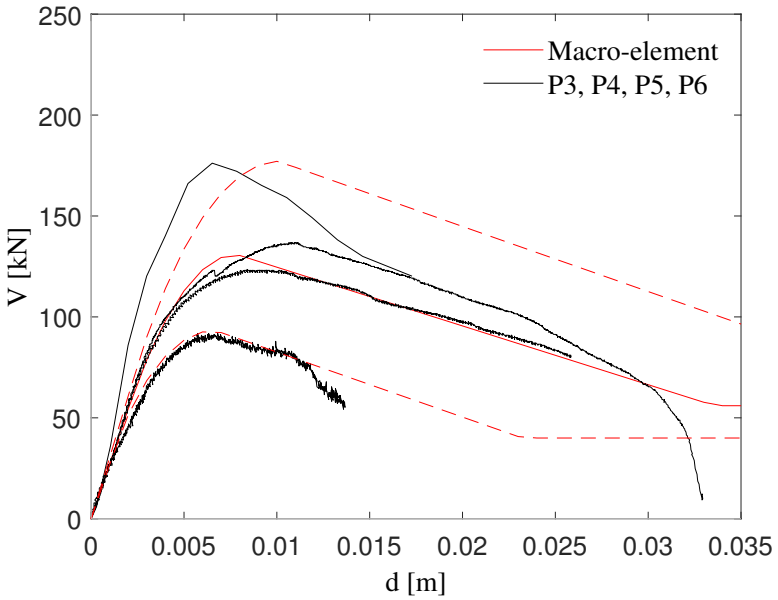


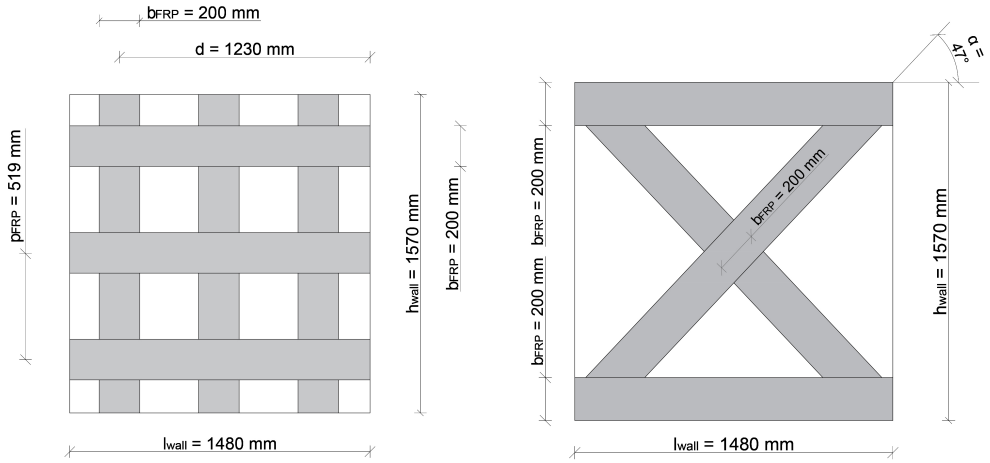
Figure 5. Resulting output from our model for the simulation of the monotonic tests carried out by Marcari et al. [36]: unreinforced specimens. The solid red line corresponds to the mean values and the dashed red lines to the minimum and maximum values of the mechanical properties.

Next, the strengthened specimens were tested using two different reinforcement layouts made via 200 mm wide strips laid in either one or two ply thickness: the grid layout comprised three strips orthogonal and three parallel to the element axis per face, and the cross layout comprised two diagonal strips and two orthogonal to the element axis strips per face (Figure 6). Since these strips were at the top and bottom of the wall, we assumed that they do not affect the shear strength of the panel and serve only to prevent end debonding of the diagonal strips. Additionally, Marcari et al. [36] reported that anchoring devices were installed, so we assumed that end debonding was prevented and intermediate debonding also governed the FRP response for the grid layout. Table 4 summarizes the thickness and mechanical properties of FRP reinforcement. The reinforcement details of each specimen and the resulting values of ε_{FRP} and c_{FRP} used in the simulations are given in Table 5.

Table 4. FRP material properties of the reinforcement used in the test campaign by Marcari et al. [36].

Type of FRP	Ply Thickness [mm]	E_{FRP} [GPa]	ε_{FRP} [%]
Glass	0.110	66	2.0
Carbon	0.167	230	1.5

In the experimental campaign, a one-ply reinforcement led to shear failure, while a two-ply reinforcement led to a shear-flexure response. For the eight walls with FRP-strengthening, Figures 7–10 compare the experimental and the numerical force–displacement curves. For each panel, three simulations were carried out using the set of mean, maximum and minimum values for the material parameters obtained from fitting the unstrengthened reference specimens. If this modelling approach works well and if the reference specimens represent the full range of masonry properties, we expect the experimental force–displacement curve of the strengthened panel to lie in the range of the three numerical simulations. This applies for most cases.

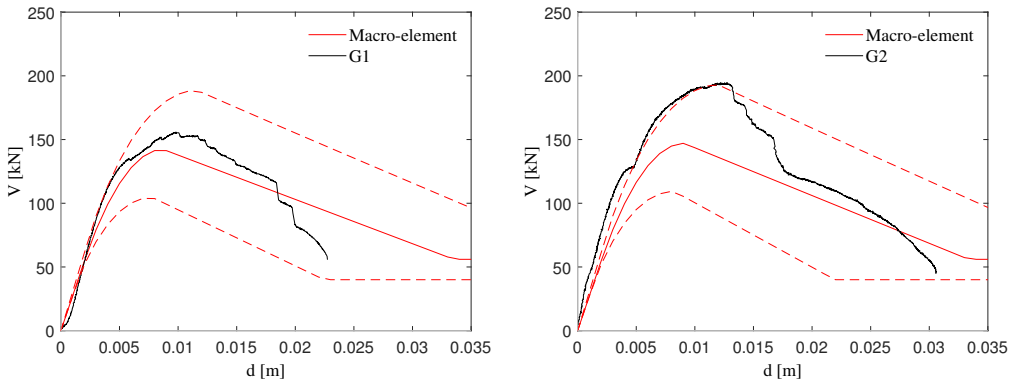


(**a**) (**b**)

Figure 6. Reinforcement layouts used in the test campaign by Marcari et al. [36] labelled as (**a**) grid or (**b**) diagonal.

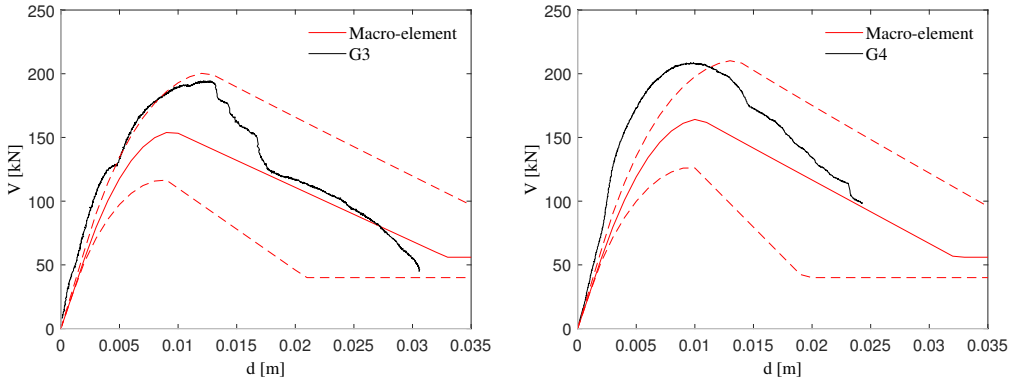
Table 5. Details of the FRP reinforcements of the eight reinforced walls [36] and the computed values for cohesion and effective strain used for the numerical simulations of the reinforced specimens.

Specimen	Fibre Type	Layout	Density	ε_{FRP} [%]	c_{FRP} [MPa]
G1	Glass	Cross	1 ply	0.574	0.0145
G2	Glass	Cross	2 ply	0.406	0.0205
G3	Glass	Grid	1 ply	0.574	0.0302
G4	Glass	Grid	2 ply	0.406	0.0427
C1	Carbon	Cross	1 ply	0.249	0.0333
C2	Carbon	Cross	2 ply	0.176	0.0472
C3	Carbon	Grid	1 ply	0.249	0.0694
C4	Carbon	Grid	2 ply	0.176	0.0983



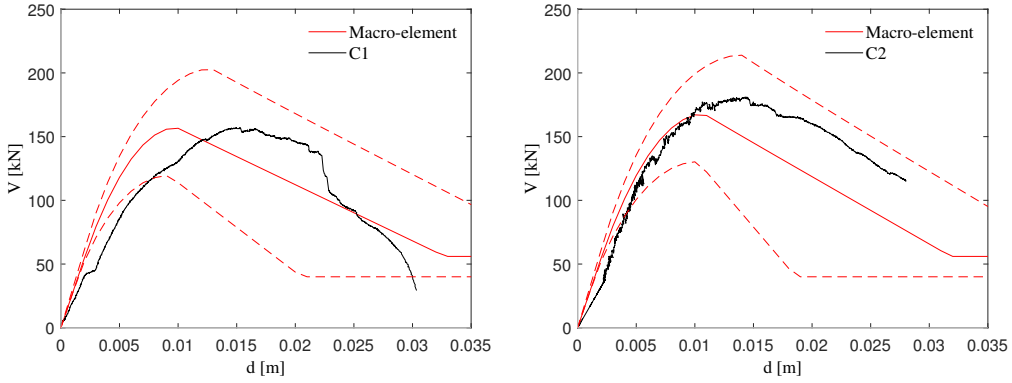
(**a**) (**b**)

Figure 7. Resulting output from our model for the simulation of the monotonic tests carried out by Marcari et al. [36]: specimens reinforced with GFRP in cross layout with (**a**) one-ply (low fibre density) or (**b**) two-ply (high fibre density). The solid red line corresponds to the mean values and the dashed red lines to the minimum and maximum values of the mechanical properties.



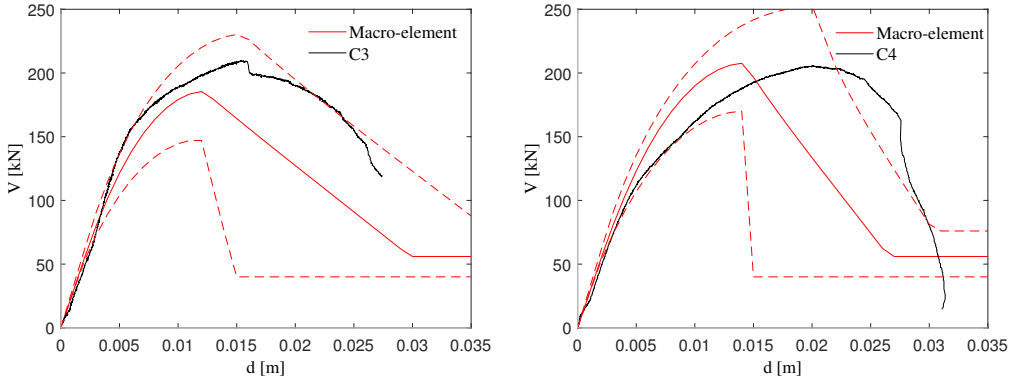
(**a**) (**b**)

Figure 8. Resulting output from our model for the simulation of the monotonic tests carried out by Marcari et al. [36]: specimens reinforced with GFRP in grid layout with (**a**) one-ply (low fibre density) or (**b**) two-ply (high fibre density). The solid red line corresponds to the mean values and the dashed red lines to the minimum and maximum values of the mechanical properties.



(**a**) (**b**)

Figure 9. Resulting output from our model for the simulation of the monotonic tests carried out by Marcari et al. [36]: specimens reinforced with CFRP in cross layout with (**a**) one-ply (low fibre density) or (**b**) two-ply (high fibre density). The solid red line corresponds to the mean values and the dashed red lines to the minimum and maximum values of the mechanical properties.



(**a**) (**b**)

Figure 10. Resulting output from our model for the simulation of the monotonic tests carried out by Marcari et al. [36]: specimens reinforced with CFRP in grid layout with (**a**) one-ply (low fibre density) or (**b**) two-ply (high fibre density). The solid red line corresponds to the mean values and the dashed red lines to the minimum and maximum values of the mechanical properties.

The force–displacement curves for specimens strengthened with glass fibres in cross and grid layouts are shown in Figures 7 and 8. The experimental data [36] can be seen in black. The red curves are numerically obtained. The mean value of the material parameters obtained from fitting the unstrengthened reference specimen is represented by the full red curve. The minimum and maximum material parameters are represented by dashed red curves, indicating that the experimental curve of the strengthened panel is within the range of the three numerical models.

Likewise, Figures 9 and 10 show masonry panels reinforced with carbon fibres.

The experimental force–displacement curve of the reinforced panel falls within the range of the three numerical simulations which suggests that the modelling approach can capture the effect of FRP strengthening.

Table 6 compares the experimental peak forces with those obtained from the simulations with the mean, minimum and maximum material parameters. The error is computed with respect to the simulation with the mean parameters.

Table 6. Comparison of the experimental and numerical peak forces for the monotonic in-plane tests by Marcari et al. [36]. F_{num} is obtained with the mean material parameters, and the range corresponds to the simulations with the minimum and maximum parameters.

Specimen	F_{exp} [kN]	F_{num} [kN]	Range [kN]	F_{num}/F_{exp}	Error [%]
G1	155.8	141.3	103.9–188.3	0.907	−9.3
G2	194.4	147.1	109.3–192.9	0.757	−24.3
G3	194.3	153.9	116.5–200.3	0.792	−20.8
G4	208.5	164.1	126.1–210.2	0.787	−21.3
C1	157.2	156.6	119.4–202.5	0.996	−0.4
C2	181.2	167.1	130.2–213.9	0.922	−7.8
C3	209.5	185.4	147.0–230.2	0.885	−11.5
C4	205.6	207.6	170.0–254.2	1.010	+1.0

4.2. Quasi-Static Cyclic In-Plane Tests

Next, we apply our developed model to the quasi-static and dynamic cyclic tests performed by ElGawady et al. [32] on unstrengthened and strengthened masonry walls. The quasi-static tests are modelled in this section and the dynamic ones in the following section. In these tests, quasi-static cyclic experiments were carried out on half-scale hollow clay block masonry walls retrofitted on only one side. Different strengthening techniques were applied, though keeping with the scope of this paper, we only modelled the two walls that were first tested in their unstrengthened configuration and then retrofitted with glass FRP. In addition to these specimens, another panel strengthened with aramid FRP was tested, but due to issues with the test setup that affected the results, it is not included here. Masonry specimens and testing procedure are described in Appendix A. Geometry and boundary conditions are shown in Figure 11.

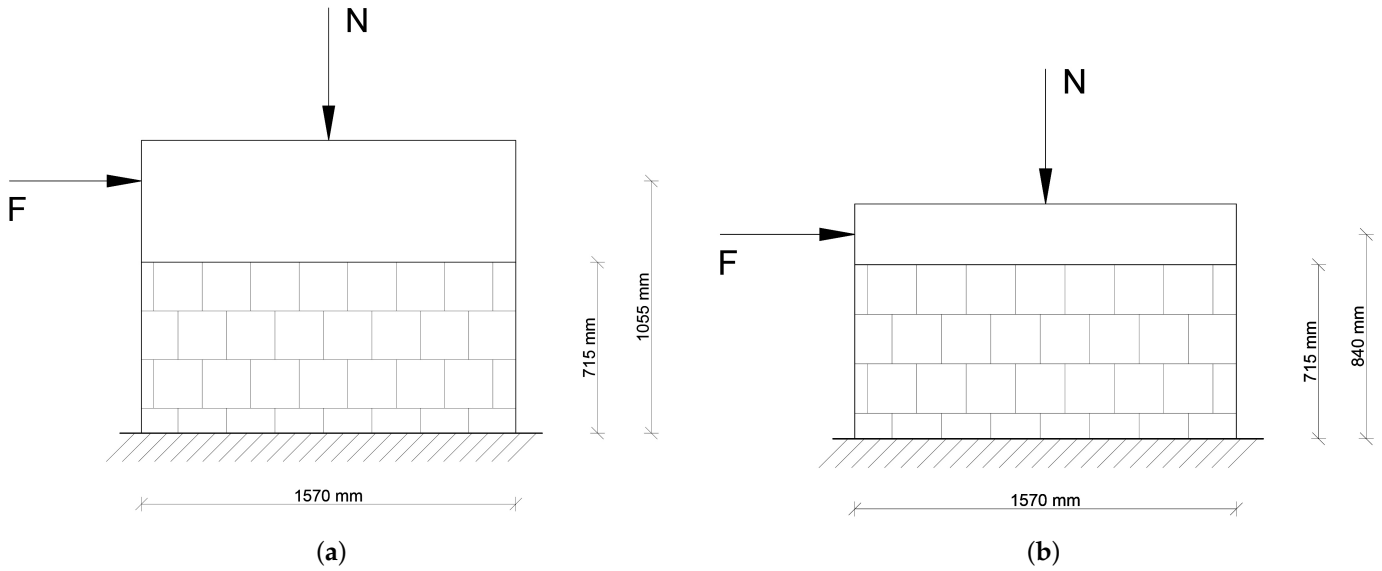


Figure 11. Boundary conditions of the walls tested in the quasi-static cyclic in-plane tests experimentally performed by ElGawady et al. [32]. (**a**) Control specimen S2-REFE-ST and (**b**) control specimen M2-REFE-ST.

ElGawady et al. [32] determined the elastic modulus of the masonry E for each wall from a vertical load test performed before the quasi-static cyclic test. For this purpose, a normal force of approximately 35 kN (0.3 MPa) was applied, and the vertical shortening at the top of the wall was measured. From these tests, an average E-modulus of 4500 MPa was determined. The characteristic compression strength of the masonry was 4.8 MPa [32]. The shear modulus was not determined experimentally, with ElGawady et al. [32] instead assuming a G-value of 40% of E. In our simulations, we assumed that G is $0.25E$ (Section 3.3). Experimentally, the cohesion was calculated to be 0.16 MPa. The coefficients of friction μ_0 and μ_R as well as the parameters G_c and δ_u [%] were calibrated to match the force–displacement hysteresis of the reference specimens S2-REFE-ST and M2-REFE-ST (see Section 3.3). The corresponding values are summarised in Table 7.

Table 7. Resulting output from our model for the simulation of the quasi-static tests by ElGawady et al. [32]: Calibrated parameters for two reference specimens.

Specimen	f_c [MPa]	E [MPa]	G [MPa]	μ_0	μ_R	G_c	c [MPa]	δ_u [%]
S2-REFE-ST	7.02	2360	590	0.39	0.2	6	0.11	0.7
M2-REFE-ST	4.8	3050	760	0.4	0.2	2	0.12	0.07

Table 8 compares the experimental and numerical peak forces in the positive and negative loading directions. The error is computed as $(|F_{num}| - |F_{exp}|)/|F_{exp}|$ for each direction.

Table 8. Comparison of the experimental and numerical peak forces in the positive and negative loading directions for the strengthened specimens of the quasi-static cyclic tests by ElGawady et al. [32].

Specimen	F_{exp} [kN]	F_{num} [kN]	Error + [%]	Error − [%]
S2-WRAP-G-F-ST	+46.5/−55.2	+66.0/−66.0	+41.9	+19.6
M2-WRAP1-G-F-ST	+68.6/−72.0	+68.4/−57.0	−0.3	−20.8

The reference specimens S2-REFE-ST and M2-REFE-ST were then retrofitted and retested with glass fibres as S2-WRAP-G-F-ST and M2-WRAP1-G-F-ST. When modelling the retrofitted specimens, we neglected the damage caused by the previous tests on the

unstrengthened walls since the masonry parameters were calibrated on the undamaged walls. The cracks were not repaired before retrofitting, and only three damaged bricks of specimen S2-REFE-ST were replaced [32]. According to ElGawady et al. [32], the FRP restored the initial stiffness of the damaged wall. However, the existing cracks may create strain concentrations in the FRP and lead to an earlier rupture, so the model may overestimate the peak force of pre-damaged walls. The modulus of elasticity of GFRP is 70 GPa, as per ElGawady et al. [32]. Since the panels were strengthened over one full surface, both shear and flexural capacity increased. The ends of the FRP strips were clamped to the footing and the head beam, which prevented end debonding. When calculating the effective maximum strain of the FRP reinforcement, we therefore assumed that intermediate debonding controlled the FRP-reinforcement response (Section 3.1). The parameters that we used in the numerical model are summarised in Table 9.

Table 9. From the experiments in ElGawady et al. [32]: FRP reinforcements of the two reinforced walls and the computed values for cohesion and effective strain used for the numerical simulations of the reinforced specimens.

Specimen	Fibre	Ply Thickness [mm]	Layout	ε_{FRP} [%]	c_{FRP} [MPa]
S2-WRAP-G-F-ST	Glass	0.06	Full surface	1.3	0.32
M2-WRAP-G-F-ST	Glass	0.06	Full surface	1.3	0.32

Figures 12 and 13 compare the numerically obtained hysteresis curves of the unreinforced and retrofitted specimens to the experimental data.

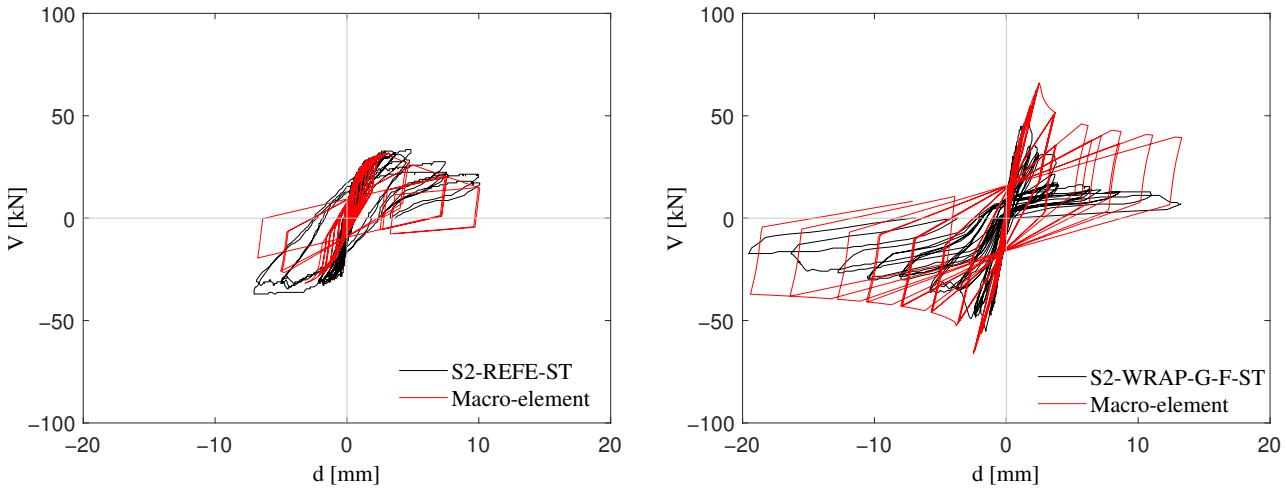


Figure 12. Resulting output from our model for the simulation of the quasi-static cyclic tests carried out by ElGawady et al. [32]: (**a**) control specimen S2-REFE-ST and (**b**) specimen retrofitted with GFRP S2-WRAP-G-F-ST.

Specimen S2-WRAP-G-F-ST experienced a rocking failure mode with masonry crushing at the toe. The rupture of FRP was induced via the vertical cracks that developed in the substrate. In the experimental campaign, the *M* specimen was not tested up to the ultimate drift because it was retrofitted and retested as M2-WRAP1-G-F-ST. In this configuration, sliding between the wall and the foundation occurred after the FRP strips ruptured. The model cannot capture this mechanism since the FRP contribution to the shear strength is introduced as a constant cohesion that is not lost when the FRP ruptures. The model therefore predicts the initial stiffness and the peak force of this specimen, but

not its post-peak response. For walls in which sliding or FRP rupture governs the post-peak behaviour, the approach should only be used to estimate the strength.

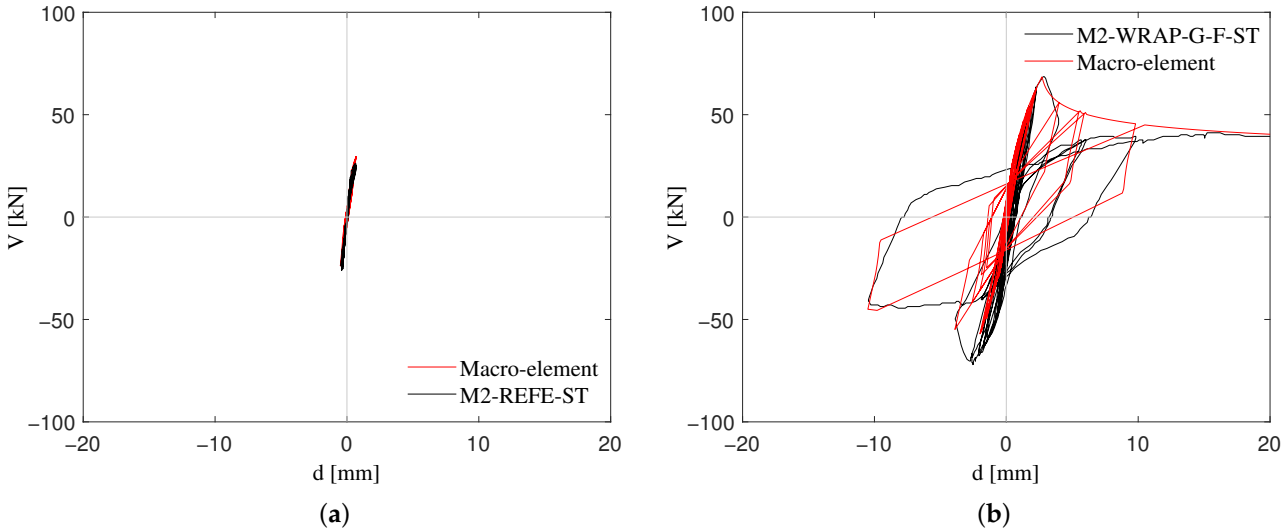


Figure 13. Resulting output from our model for the simulation of the quasi-static cyclic tests carried out by ElGawady et al. [32]: (**a**) control specimen M2-REFE1-ST and (**b**) specimen retrofitted with GFRP M2-WRAP1-G-F-ST.

4.3. Dynamic In-Plane Tests

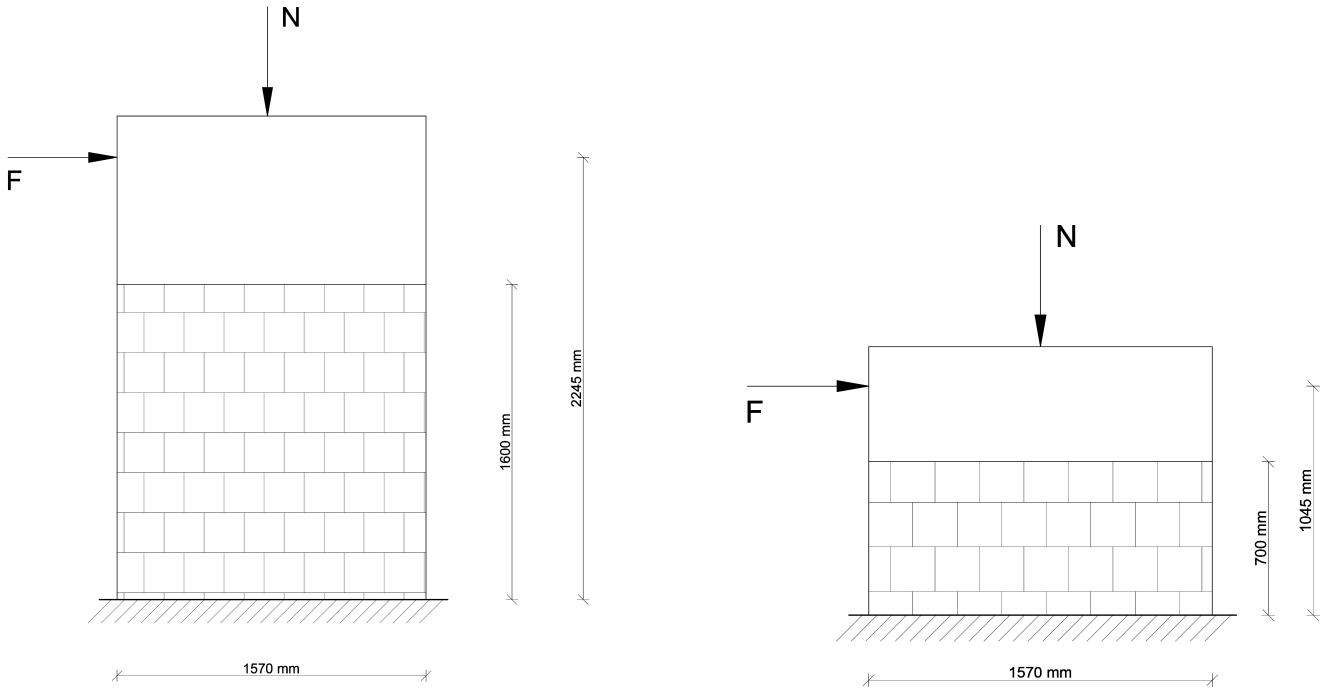
In addition to the quasi-static cyclic tests on FRP-strengthened walls presented and modelled in the previous section, ElGawady et al. [33] also investigated the in-plane behaviour of FRP-strengthened hollow clay block masonry walls under dynamic loading. This campaign included three half-scale unreinforced control specimens that were later retrofitted and retested. To investigate an increase in only flexural capacity, one additional specimen was built with vertical carbon plates along the edges, though this specimen is not included here.

Boundary conditions of the tested walls are shown in Figure 14. A further description of geometry and testing campaign is presented in Appendix A.

The compressive strength (5.7 MPa and 7.17 MPa) and the Young's modulus (4500 MPa) of the masonry was determined through the same procedure described in the previous subsection. The input parameters to the macro-element were fitted for three reference panels without reinforcement following the approach described in Section 3.3. Table 10 summarises the obtained material values for the three reference panels.

Table 10. Resulting output from our model for the simulation of the dynamic tests carried out by ElGawady et al. [33]: Calibrated parameters for three reference specimens.

Specimen	f_c [MPa]	E [MPa]	G [MPa]	μ_0	μ_R	G_c	c [MPa]	δ_u [%]
L1-REFE	6.00	1500	540	0.40	0.20	6	0.10	0.73
S1-REFE	6.58	1250	310	0.40	0.20	3.5	0.11	1.0
S2-REFE	6.33	1270	310	0.45	0.30	3.5	0.12	1.0



(**a**) (**b**)

Figure 14. Boundary conditions of the tested walls: control specimens of the (**a**) slender type (L specimens) and (**b**) squat type (S specimens) [33].

Table 11 compares the experimental and numerical peak forces in both loading directions, with the error computed as for the quasi-static tests.

Table 11. Comparison of the experimental and numerical peak forces in the positive and negative loading directions for the strengthened specimens of the dynamic tests by ElGawady et al. [33].

Specimen	F_{exp} [kN]	F_{num} [kN]	Error + [%]	Error − [%]
L1-WRAP-G-F	+50.0/−65.2	+58.1/−59.1	+16.2	−9.4
S1-WRAP-G-F	+72.7/−75.3	+66.8/−82.5	−8.1	+9.6
S2-WRAP-A-F	+35.1/−36.0	+31.3/−33.4	−10.8	−7.2

The seismic response of the walls is significantly affected by the level of damping. To avoid over-damping of long period oscillations typical of higher levels of nonlinearity with typically lower damping ratios, here a Rayleigh damping model was used that is directly proportional to the mass and initial stiffness [16]. The uncertainty in the damping ratio was investigated through a sensitivity analysis. The best matching results are obtained for damping ratio 2.5% and are presented in the following Figures 15–17. Finally, some of the unstrengthened specimens did not reach their displacement capacity since the testing was stopped prematurely to also test these specimens in a strengthened configuration.

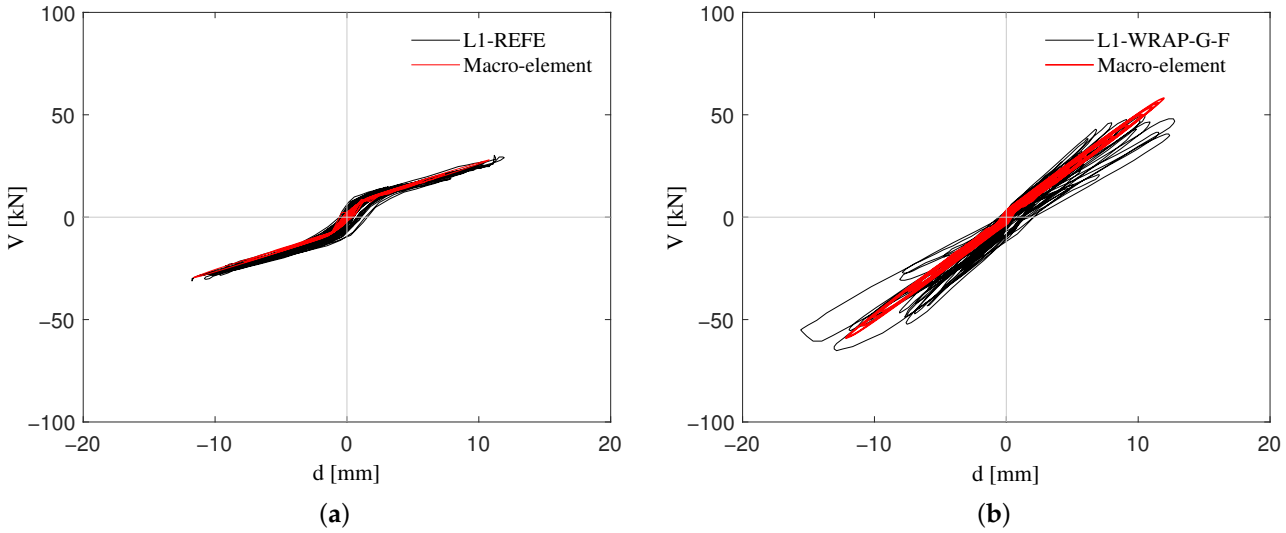


Figure 15. Resulting output from our model for the simulation of the dynamic tests carried out by ElGawady et al. [33]: (**a**) control specimen L1-REFE and (**b**) specimen retrofitted with GFRP L1-WRAP-G-F.

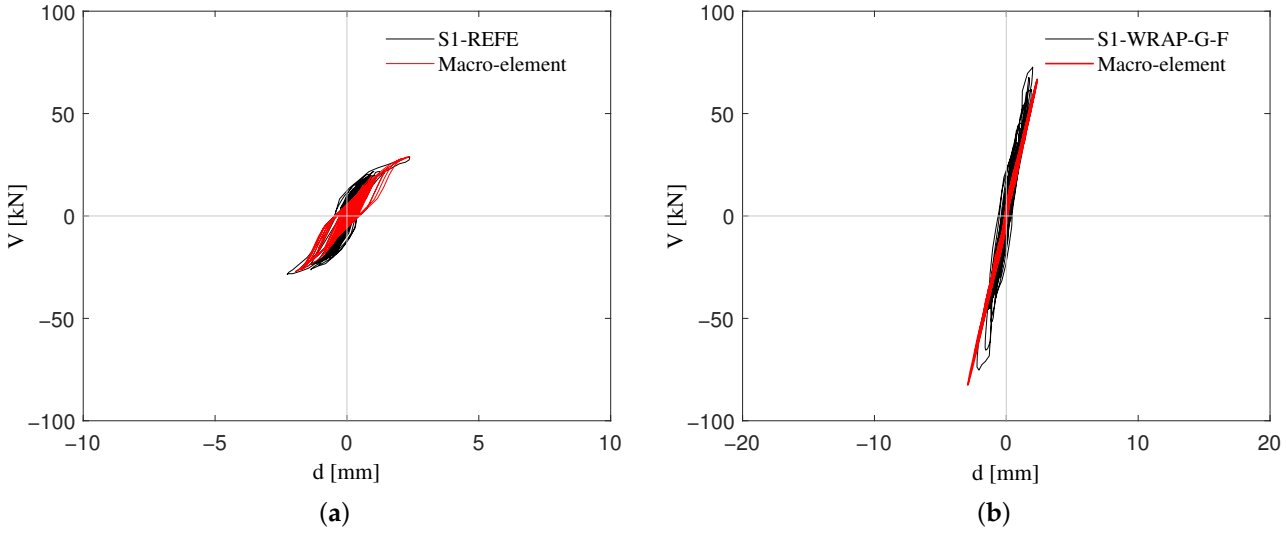
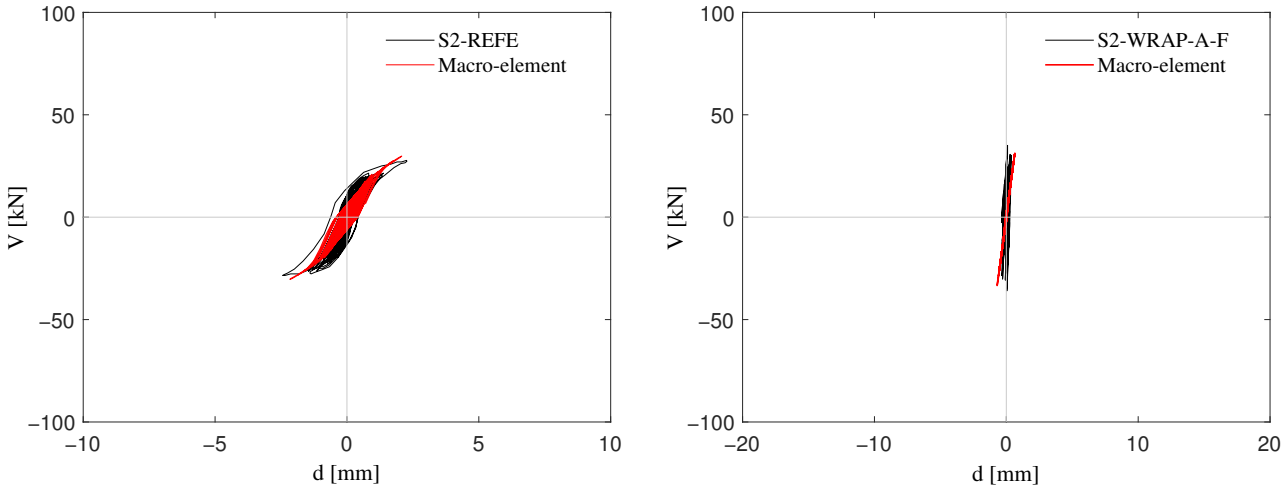


Figure 16. Resulting output from our model for the simulation of the dynamic tests carried out by ElGawady et al. [33]: (**a**) control specimen S1-REFE and (**b**) specimen retrofitted with GFRP S1-WRAP-G-F.

After testing the URM specimens, only one side of each wall was retrofitted over its full surface with glass and aramid fibres. To avoid anchorage failure, polymers were clamped at the bottom and at the top of the specimen with steel plates and screw bolts. Table 12 provides the mechanical properties for the polymer materials used for retrofitting. Table 13 describes the retrofitted specimens in terms of applied composite material and the parameters used in the numerical simulations.



(**a**) (**b**)

Figure 17. Resulting output from our model for the simulation of the dynamic tests carried out by ElGawady et al. [33]: (**a**) control specimen S2-REFE and (**b**) specimen retrofitted with AFRP S2-WRAP-A-F.

Table 12. FRP properties used in experimental campaign of dynamic tests [33].

Commercial Name	Fibre Type	E [GPa]	ε_u [%]
SikaWrap-400A 0/90	Aramid	100	2.8
SikaWrap-300G 0/90	Glass	70	3.0

Table 13. Details of FRP-reinforcements of the three reinforced walls in the dynamic tests [33] and computed values for cohesion and effective strain that were used for the numerical simulations of the reinforced specimens.

Name	Fibre Type	Layout	ε_{FRP} [%]	c_{FRP} [MPa]
L1-WRAP-G-F	Glass	Full surface	1.71	0.57
S1-WRAP-G-F	Glass	Full surface	1.71	0.57
S2-WRAP-A-F	Aramid	Full surface	1.27	0.61

Figures 15–17 show the force–displacement curves of the experimental and numerical analyses. Here, there is a good agreement between the initial stiffnesses attained experimentally and numerically. Moreover, the forces and displacements are also comparable. However, it is important to highlight the fundamental influence of damping when modelling dynamic analyses. These results support our hypothesis that it is possible to perform simplified modelling of the strengthening applied to the macro-element.

4.4. Out-of-Plane Bending Tests

Next, we validated the ability of our modelling approach to reproduce the out-of-plane response of FRP-strengthened masonry walls. To do this, we modelled the experimental work of Triantafillou [30], who tested six masonry wallets of perforated clay bricks reinforced with externally bonded polymers. The tests were four-point bending tests. The experimental campaign and specimens are described in detail in Appendix A. Two specimens were unreinforced reference specimens, while the other four were reinforced with either two or four carbon strips (0.1 mm thick and 50 mm wide) on the side engaged in

tension. The masonry compressive strength (3.57 MPa) and elastic modulus (3.80 GPa) were determined from uniaxial tests.

It is reported in Triantafillou [30] that the control specimens failed at a force of 4.05 kN and 4.70 kN, though the curves were not provided. Specimens reinforced with two carbon strips were named Wall 02a and Wall 02b, while specimens reinforced with four strips were named Wall 04a and 04b. See Table 14 for a summary of the material properties for the tests and Table 15 for the properties used for the OpenSEES analyses.

Table 14. FRP material properties of the reinforcements used in the test campaign by Triantafillou [30].

Fibre Type	E [GPa]	Ply Thickness [mm]
Carbon	150	0.1

Table 15. Resulting output from our model for the simulation of the four-point bending test carried out by Triantafillou [30]: Calibrated parameters for reference specimens.

E [GPa]	G [GPa]	μ_0	μ_R	G_c	c [MPa]
3.8	0.95	0.4	0.2	6	0.09

Curves given in Figure 18 present load vs. midspan displacement and show that the simplified numerical approach well predicts the maximum force reached and the displacement capacity. However, for the initial stiffness, one of the specimens retrofitted with a higher reinforcement ratio slightly disagreed with experimental results.

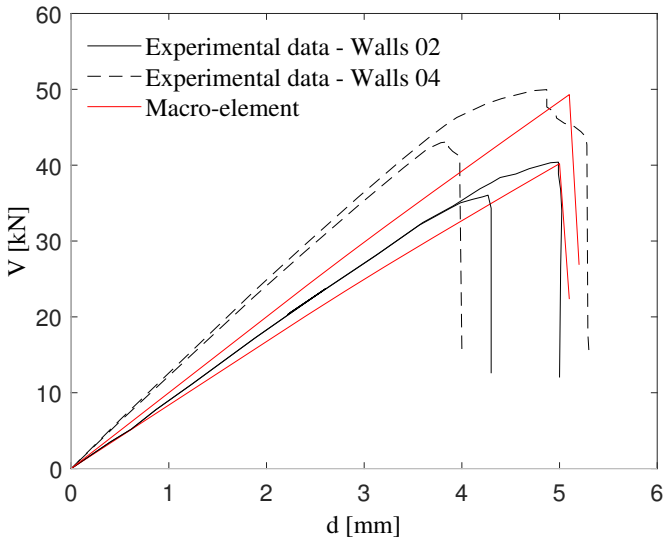


Figure 18. Resulting output from our model for the simulation of the out-of-plane bending tests carried out by Triantafillou [30]: retrofitted specimens Walls 02 and Walls 04.

Specimens failed by crushing of the masonry in compression. Table 16 presents a comparison of failure loads and initial stiffnesses for the experimental, theoretical and numerical results.

Table 16. Comparison of the experimental, theoretical (from [30]) and numerical output from our model for the out-of-plane bending tests.

Specimen	F_{exp} [kN]	F_{the} [kN]	F_{num} [kN]	F_{num}/F_{exp}	Error F_{num} [%]	k_{intnum}/k_{intexp}
Wall 02a	40.40	41.53	40.2	0.9950	−0.5	0.9071
Wall 02b	36.05	41.53		1.1151	+11.5	0.9071
Wall 04a	43.10	48.59	49.3	1.1439	+14.4	0.8234
Wall 04b	49.95	48.59		0.9870	−1.3	0.7973

Note: Walls 02a and 02b, and Walls 04a and 04b, are nominally identical specimens. Each pair is therefore represented by a single numerical model, and the numerical result is compared with each experimental result separately.

5. Modelling Hypothetical FRP-Strengthening Interventions for a Case Study Building

The advantage of macro-element modelling is that numerous dynamic analyses can be performed with a low computational effort and in a reasonably short time. This allows investigating the strengthening effect on both the global and the local behaviour of a building.

Since shake table tests on large-scale buildings are characterised by a high cost and complexity, it is not surprising that there is a limited number of experimental campaigns addressing the behaviour of strengthened URM buildings tested on the shake table. The building tested on the shake table and retrofitted with diagonal CFRP by Tomaževič [70] did not exhibit out-of-plane failure. A single-storey building was designed by Saleem et al. [71], where only GFRP parallel to the element axis was applied. Krstevska et al. [72] presented an overview of scaled FRP-retrofitted historical buildings tested on a shake table. However, churches and mosques, due to their complex geometry, are difficult to model using EFM. Gu et al. [73] tested a three-floor masonry wall at one-third scale with openings, strengthened with CFRP grid. However, the test was performed under quasi-static loading. The same testing procedure was used in Triller et al. [74], where a full scale three-storey structure was strengthened with GFRCM.

To illustrate how our herein developed and validated modelling approach for FRP-strengthened masonry walls can be used to assess potential retrofit solutions on the building level, we analyse hypothetical retrofit solutions of a building that was tested dynamically in its unretrofitted configuration. For this purpose, we selected the CoMa-WallS building, which is a mixed reinforced concrete and unreinforced masonry structure [29]. The structure has been modelled in its unretrofitted configuration in Vanin et al. [16]. Since only the unstrengthened configuration was tested, the results of the strengthened configurations presented in this section are numerical predictions that illustrate the application of the approach and have not been validated experimentally.

We chose this building because it exhibited out-of-plane failure in the top storey and in-plane failures in the first and second storey when tested on a uni-directional shake table. The out-of-plane failure of the top-floor wall was also treated in Tondelli et al. [75], where the out-of-plane loaded wall was modelled using discrete elements. Vanin et al. [16] proved that it is possible to capture the onset of local failure through an EFM. We reuse here this model of the unreinforced configuration and model hypothetical retrofit interventions. All slabs were reinforced concrete slabs and modelled as elastic shell elements since they provided a significant out-of-plane bending stiffness. The concrete walls were modelled using force-based beam elements, while URM walls were represented by macro-element that was also used for modelling the FRP-strengthened walls in Sections 4.1–4.4. Masonry compressive strength was calibrated as 5.66 MPa and the elastic modulus as 4500 MPa by Vanin et al. [16], based on shear–compression tests on walls of the same masonry.

For in-plane loading, drift limits of 0.95% for shear failure and 1.34% for flexural failure were set, as reported in [29,76] for the near collapse limit state. The testing sequence included nine ground motions obtained by scaling the ground motion of the Montenegro earthquake (1979). This broad-band frequency content record was registered at the Ulcinj-Hotel Albatros station during the 15 April 1979 earthquake [29]. The direction along which the unidirectional motion was applied is N-S, exposing two URM walls to out-of-plane loading. Note that unlike in Vanin et al. [16] we carry out the analyses using the recently developed secant-stiffness proportional damping model [77]. This new secant-damping model avoided the common overdamping of rocking motions observed with initial-stiffness proportional damping [77]. The damping model was calibrated using the periods T_1 of the first mode and three times T_1. A 1% damping ratio was chosen because it predicts the global response better in the unstrengthened configuration than a 2% damping ratio [16].

The numerical models included three hypothetical strengthening configurations. The first configuration contained carbon fibres applied in a diagonal layout on both sides of the wall; strengthening was applied only to walls perpendicular to the direction of the seismic loading, meaning only on the walls subjected to out-of-plane deformations (RetrConfig A, Figure 19). In the second configuration, the FRP type and layout were applied on all the walls, however, the fibres were not anchored in the slab (RetrConfig B). In the third configuration, regardless of whether the walls were loaded in-plane or out-of-plane, they were all reinforced with FRP and anchored in the slab (RetrConfig C, Figure 19).

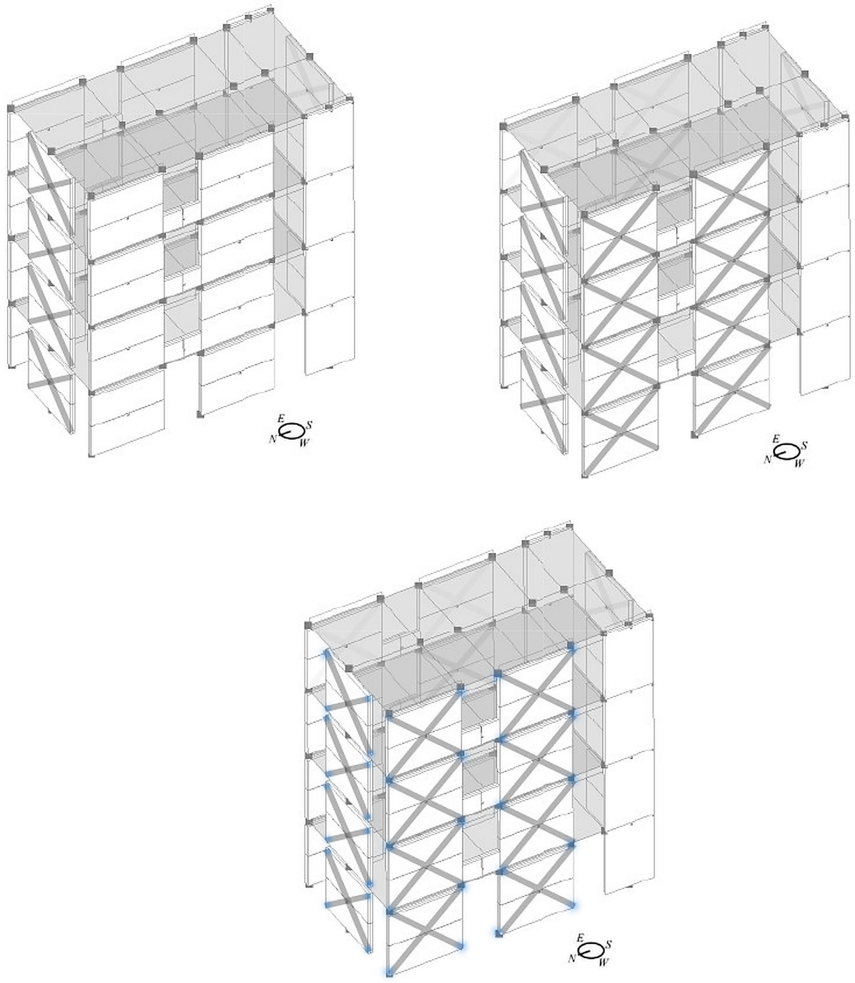


Figure 19. Equivalent frame model of the building tested by Beyer et al. [29], modelled in unstrengthened configuration by Vanin et al. [16], with applied RetrConfig A, RetrConfig B and RetrConfig C.

The properties of CFRP used in the numerical models are presented in Table 17. When modelling the fibres anchored to the slab, all three sections of the macro-element were reinforced (bottom, middle and top section). However, when anchorage devices were missing, it was assumed that the FRP-strengthening has only an effect on the shear strength and on the flexural strength of the middle section, i.e., it was assumed to not influence the flexural strengths of the end sections of the macro-element. Incremental dynamic analyses were performed applying as in the experimental campaign the Montenegro record in the NS direction of the building. Since a single record was used, these analyses are intended to illustrate how the proposed approach can be used to compare retrofit solutions, and not to provide a generalisable capacity assessment of the building.

Table 17. FRP material properties of the reinforcement.

Fibre Type	E [GPa]	Ply Thickness [mm]	Layout	ε_{FRP} [%]	c_{FRP} [MPa]
Carbon	234.5	1.8	Diagonal	0.15	1.28

Figure 20 compares the out-of-plane displacement of the middle section of the top storey wall of the unretrofitted configuration (i.e., the configuration that was tested experimentally) and the proposed strengthened configuration. The model predicts that the FRP limits the out-of-plane displacements of this wall. This suggests that local out-of-plane failures could be prevented through the use of composites, ensuring the global response of the building.

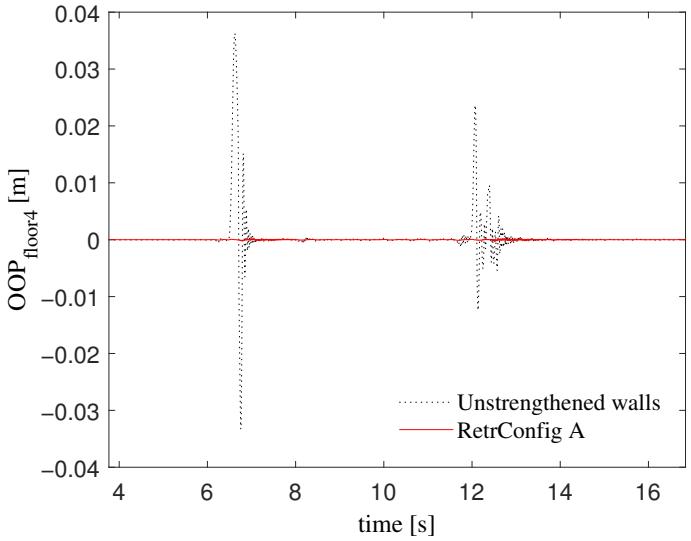


Figure 20. Resulting output from our model for the simulation of the shake table tests by Beyer et al. [29], modelled in unstrengthened Vanin et al. [16] and in RetrConfig A: Comparison of the time-history responses for Run 9 of the out-of-plane deformation at midheight of the out-of-plane loaded URM wall flanked by URM walls, at the top story.

Models RetrConfig B and RetrConfig C are built to show the effect of strengthening on the global response of the building. Figure 21 plots the IDA curves for the maximum absolute displacements of the top floor. The maximum displacement is significantly reduced after applying CFRP, even if the CFRP is not anchored in the slabs (RetrConfig B). Furthermore, when the CFRP is anchored in the slabs and therefore the top, bottom and middle section are reinforced (RetrConfig C), the PGA that the building can withstand is greater than when only the middle section is reinforced. In addition, the failure mode changed from flexure to shear.

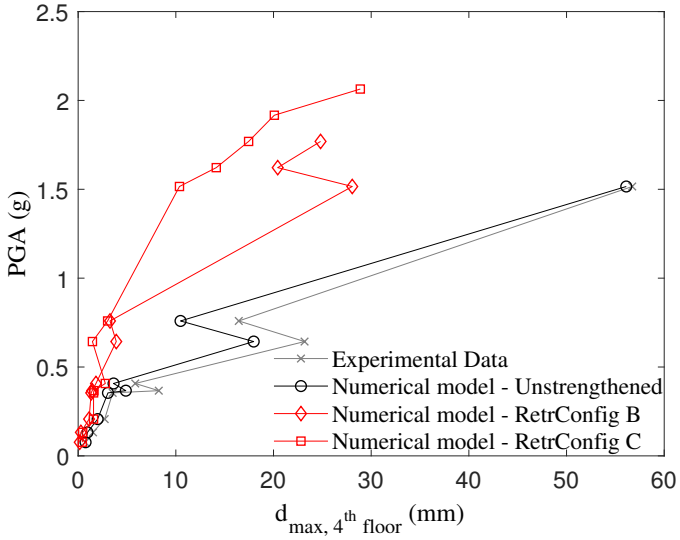
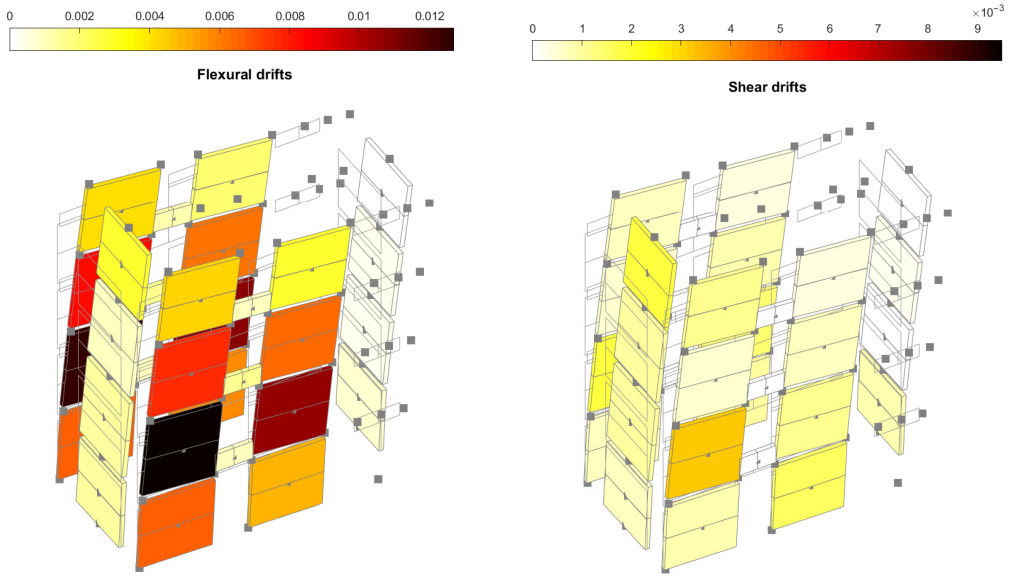


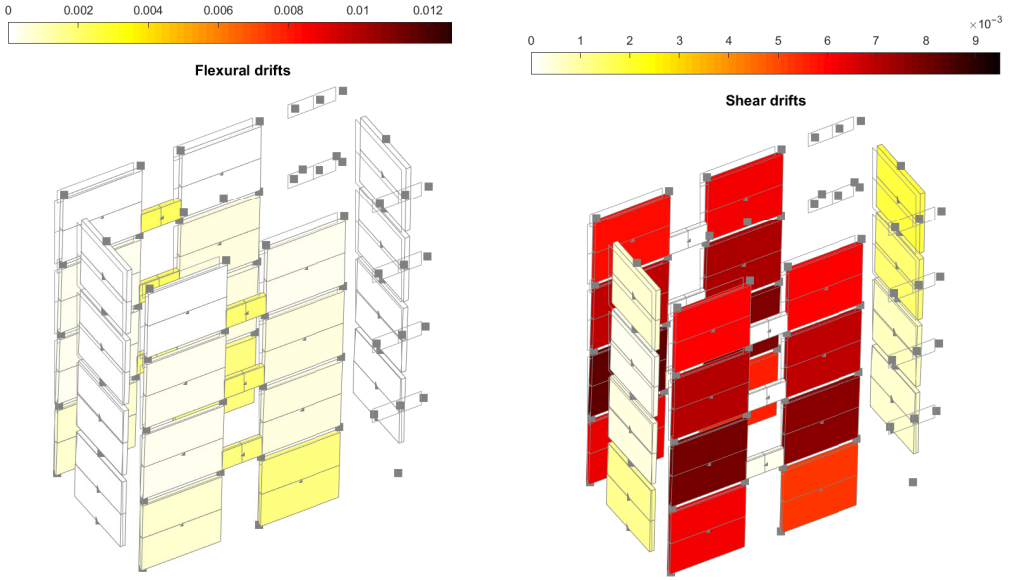
Figure 21. Resulting output from our model for the simulation of the shake table tests by Beyer et al. [29], modelled in unstrengthened Vanin et al. [16] and RetrConfig B and RetrConfig C. Comparison of the global response in terms of maximum displacements.

The effect of the retrofitting solutions was also visible when the deformation demands in terms of shear and flexural deformation at failure were examined, as shown in Figures 22 and 23. The displacements are amplified by a factor of 10. The good distribution of drift demands over the height of the building results from the coupling with the RC walls and was also observed in the experimental test of the unstrengthened configuration.



(**a**) (**b**)

Figure 22. Deformed shape and maximum element drifts in flexure (**a**) and in shear (**b**) for RetrConfig B for a PGA of 1.76 g. Only the element drifts of the masonry walls are plotted.



(**a**) (**b**)

Figure 23. Deformed shape and maximum element drifts in flexure (**a**) and in shear (**b**) for RetrConfig C for a PGA of 2.06 g. Only the element drifts of the masonry walls are plotted.

6. Applicability, Limitations and Future Research

6.1. Applicability

The proposed approach was validated for regular masonry with a well-defined cross-section, namely tuff masonry [36], hollow clay block masonry [32,33] and perforated clay brick masonry [30]. It was then applied to a building with modern clay brick masonry walls [29]. The validated strengthening schemes include carbon, glass and aramid FRP in grid, diagonal and full-surface layouts, applied on one or both faces of the wall. In the validation campaigns, the FRP ends were anchored or clamped, so the validation does not cover walls in which debonding governs the response. The effect of anchoring the FRP in the slabs was investigated only in the case study building (Section 5) and was not compared with experimental results. The stone walls tested by Marcari et al. [36] were multi-leaf panels with a partial connection between the external leaves, strengthened on both faces. For these walls, the assumption of a monolithic cross-section in the fibre section led to a good agreement with the experimental results. However, the approach has not been validated for multi-leaf walls with a weak infill core. In such cases, leaf separation cannot be captured and the FRP may not influence the full wall thickness. Finally, the approach was validated for piers but not for strengthened spandrels.

6.2. Limitations

The macro-element builds on the assumption that plane sections remain plane, so the FRP and masonry fibres have the same strain and slip at the interface is not modelled. Debonding is therefore accounted for through a limit on the maximum FRP strain, which captures the strength at which debonding is expected but not the slip at the interface, the progressive debonding, the delamination within the masonry substrate or the response after debonding. Bond degradation under cyclic or environmental loading is not modelled either. The FRP is represented as linear elastic in tension up to its limit strain, with zero compressive strength, and the resin is not modelled explicitly (Section 3.1).

The drift capacities of the unstrengthened walls are retained for shear and flexural failure, and the shear stiffness is not modified, as no established models exist for the effect of strengthening on these properties. This affects only the drift at which the strength drops, not the strength or the governing failure mechanism. The assumption is conservative when the strengthening increases the deformation capacity, but it may be unconservative when FRP debonding or rupture leads to a more brittle response.

The FRP contribution to the shear strength is introduced as a constant cohesion, independent of the axial load and of the strain in the FRPs, following the engineering models [58,63]. The loss of this contribution after FRP rupture, and the sliding that may follow, therefore, cannot be captured. For the retrofitted specimens, the damage from previous tests on the unstrengthened walls was neglected, which may lead to an overestimation of the peak force when FRP rupture is induced by existing cracks.

The coefficients c_1 and k_{cr}, used to compute the debonding strain, are taken from CNR-DT 200 R1 [58]. The coefficient c_1 is provided only for a limited number of masonry types, and k_{cr} was derived from tests on reinforced concrete members and has not yet been calibrated for masonry substrates [78]. Since the effective FRP strain is proportional to $k_{cr}\sqrt{c_1}$, the uncertainty in these parameters is most relevant for heavily strengthened walls with low axial load.

As in the macro-element by Vanin et al. [13], the out-of-plane response is limited to one-way bending, so walls restrained on three or four sides are not represented accurately. The out-of-plane shear response of the macro-element is linear elastic. Since FRP strengthening increases the out-of-plane flexural capacity and therefore the shear demand, out-of-plane shear failure may become critical for heavily strengthened walls and should be verified separately. Finally, the building analyses in Section 5 were carried out with a single ground motion record, the input of the shake table test. The PGA at failure and possibly the failure modes may change for records with a different frequency content, so a probabilistic assessment with a set of ground motions is left for future research.

Therefore, the approach should be used with caution for FRP systems without end anchorage on weak or irregular substrates, where debonding may govern the response; for multi-leaf walls with a weak infill core; for walls in which out-of-plane shear or two-way bending governs; and for assessments that rely on the post-debonding or post-rupture response of the FRP.

6.3. Future Research

A similar modelling approach could be applied to fabric-reinforced cementitious matrix (FRCM) systems. Fibres representing the textile would be added to the section, and the shear contribution would be introduced through the cohesion term, with effective strains taken from CNR-DT 215/2018 [79]. However, the tensile response of FRCM is typically described by a trilinear law with an uncracked stage, a crack development stage and a cracked stage governed by the textile [80,81]. This law would need to be assigned to the reinforcement fibres instead of the linear elastic law used for FRP. FRCM systems have also been shown to increase the deformation capacity of masonry walls more than FRP [82]. The present model does not account for this, and it should be included in future developments.

Future research should also include a comprehensive sensitivity analysis of the key modelling parameters, including the coefficients k_{cr} and c_1, and a calibration of both coefficients based on FRP-to-masonry bond tests.

7. Conclusions

The objective of this paper was to develop and validate a computationally efficient method for modelling FRP-strengthened masonry buildings that considered the impact of FRP-strengthening on the in-plane and out-of-plane capacity. The proposed method is an equivalent frame model (EFM) that uses the new macro-element model developed by Vanin et al. [13], which is implemented in OpenSEES [64]. The increase in shear capacity, one of the main parameters that define the shear response of the macro-element, was simulated through an increase in cohesion computed from engineering models that predict the shear resistance of FRP-strengthened masonry walls. To compute the shear strength increase as a result of strips orthogonal to the element axis in this study, we used models of the Italian guideline Consiglio Nazionale delle Ricerche [58], and to consider diagonal strips, we used an equation by Prota et al. [63]. The increase in flexural capacity was modelled by adding fibres to the sections, which represent the FRP reinforcement. The flexural capacity of the macro-element was computed based on the assumption that plane sections remain plane. It is therefore not possible to explicitly consider debonding or delamination in the simulation, so these are accounted for through limiting the ultimate strain of the FRP-reinforcement fibres. We assumed that there is no increase in deformation capacity after applying strengthening. Our herein proposed modelling approach was validated against experimental campaigns on FRP-strengthened walls. The peak forces of the strengthened walls were predicted with errors mostly within $\pm$20%. The largest deviations occurred for specimens whose response was governed by mechanisms not represented in the model, such as sliding and FRP rupture induced by cracking of the substrate. Hence, the efficiency of the reinforcing system in enhancing in-plane and out-of-plane capacity of a masonry wall was demonstrated by numerical results. Within an EFM, the approach therefore provides a computationally efficient framework for predicting the seismic response of masonry buildings with FRP-strengthened walls. While the response of the strengthened walls was validated against experimental results, the application to the case study building was based on hypothetical retrofit configurations. Its validation at the building level requires shake table tests on strengthened buildings, which are still scarce. It is worth noting that EFMs are a reasonable choice in terms of computational burden and analysis time. As a result, EFMs allow for numerous dynamic analyses that explicitly describe parameter uncertainty. In this manner, we may predict a scenario of possible failure mechanisms and damage patterns for various types of FRP materials and retrofitting layouts. The understanding gained from studies of this type is necessary to judge the effect of an intervention on the overall building response, making this a necessary input for any force-based or displacement-based assessment methods. This approach may also be used to evaluate the performance of both retrofitted masonry and retrofitted mixed constructions. Finally, models such as the one developed herein may support the choice of a suitable strengthening approach for the retrofitting of URM buildings.

Author Contributions: Conceptualization, K.B. and F.V.; methodology, I.B. and F.V.; software, F.V.; validation, I.B.; formal analysis, I.B. and F.V.; investigation, I.B.; resources, K.B.; data curation, I.B.; writing—original draft preparation, I.B.; writing—review and editing, K.B.; visualization, I.B.; supervision, K.B.; project administration, K.B.; funding acquisition, K.B. All authors have read and agreed to the published version of the manuscript.

Funding: The project was supported by the Swiss National Science Foundation through grant 200021_175903/1 *Equivalent frame models for the in-plane and out-of-plane response of unreinforced masonry building.*

Data Availability Statement: All files for computing the macro-element properties as well as the input and results files of the OpenSEES analyses are shared openly through the Zenodo repository

https://doi.org/10.5281/zenodo.4733243. More specifically, these files include the OpenSEES models used for producing the results presented in the papers as well as the cohesion calculation sheets and numerical analyses.

Acknowledgments: The authors thank Pierino Lestuzzi for sharing the data of the quasi-static cyclic shear–compression tests and the shake table tests reported in ElGawady et al. [32] and ElGawady et al. [33] .

Conflicts of Interest: The authors declare no conflict of interest.

Appendix A

Appendix A.1. Monotonic In-Plane Tests

Marcari et al. [36] carried out an experimental campaign on FRP-strengthened tuff masonry walls subjected to monotonic in-plane loading. The height of the panels was 1.57 m, the length 1.48 m and the thickness 0.53 m. For the test, the specimens were subjected to a monotonically increasing horizontal displacement up to failure and a constant axial load of 400 kN, which corresponds to an axial load ratio of 0.36. The specimens were fully fixed at the bottom and the rotation was fixed at the top such that the specimens were subjected to double-bending (Figure 4).

Appendix A.2. Quasi-Static Cyclic In-Plane Tests

ElGawady et al. [32] performed quasi-static and dynamic cyclic tests. The quasi-static cyclic tests were carried out on masonry walls that were 1.57 m long, 0.715 m high and 0.075 m wide with two different shear span to wall height ratios; the shear span of the *S* specimens was 1.055 m, which resulted in a shear span ratio of 0.67, while the *M* specimens were squatter with a shear span of 840 mm and corresponding shear span ratio of 0.54 (Figure 11). Cantilever boundary conditions were applied, but the horizontal jacks connected to the concrete beam on top of the wall made the shear span to wall height ratio larger than 1.0. In the numerical models, this was modelled using a rigid offset between the top node of the wall and the node where the horizontal displacement was imposed.

To generate the force, two external post-tensioning bars applied an axial force of 30 kN, while 12 kN was added from the weight of steel elements at the top of the wall, the reinforced concrete top beam and the masonry panel. In total, an axial compressive force of 42 kN was therefore applied at the top of each wall, which corresponds to an axial load ratio of 7.4%. To keep the force approximately constant during the test, springs were used with the post-tensioned bars. The horizontal load was applied manually using two uni-directional hydraulic jacks and hand pumps. Both positive and negative loading cycles were considered for determining the maximum lateral force and the ultimate displacement capacity, with one jack pushing when loading in the positive direction and the other jack pushing when loading in the negative direction. This complex setup might explain the asymmetry in the positive and negative directions of the hysteresis curves. At each displacement amplitude, three loading cycles were applied.

Appendix A.3. Dynamic In-Plane Tests

In addition, ElGawady et al. [33] carried out dynamic tests. The experiment tested walls of two different aspect ratios: slender walls were 1.6 m high with a shear span ratio of 1.4, and squat walls were 0.7 m high with a shear span ratio of 0.7. The length and the width of all specimens were 1.57 m and 0.075 m, respectively. All walls were tested as cantilever walls (Figure 14).

The shake table test setup included a horizontal moveable mass of 12 t, which was supported on rails and connected to the wall through stiff bars. The acceleration of this

mass resulted in a horizontal force that acted at 2.245 m above the foundation for the slender specimen and at 1.045 m for the squat specimen. In the finite element model, the mass of the wall was around 340 kg, which was represented by two lumped masses at the top and bottom of the wall. An additional mass of 190 kg was applied at 1.825 m above the foundation to represent the mass of the beam on top of the slender walls. For the squat walls, the mass of the top beam was 180 kg, which was applied at a height of 0.955 m. Similar to the quasi-static cyclic test (Section 4.2), the vertical load applied to the wall consisted of the weight of the wall and the top beam, the weight of steel elements at the wall top of the test setup (in total 12 kN) and a force applied by a post-tensioned bar (30 kN). During testing, the wall elongated due to the formation of flexural cracks, resulting in an increase in the force in the post-tensioned bar. To keep the axial force approximately constant during the test, springs were installed. However, despite this measure, the axial load varied considerably during the tests, so the change of axial force due to the elongation of the post-tensioned bars was modelled explicitly. Boundary conditions of the tested walls are shown in Figure 14.

Appendix A.4. Out-of-Plane Bending Tests

Triantafillou [30] tested six masonry wallets of perforated clay bricks reinforced with externally bonded polymers. The tests were four-point bending tests, and the boundary conditions were those of a simply supported beam. No axial force was applied, and the wallets were tested in a horizontal position. The wallets had a length of 900 mm, a width of 400 mm and a thickness of 120 mm.

References

1. Penna, A.; Morandi, P.; Rota, M.; Manzini, C.F.; da Porto, F.; Magenes, G. Performance of masonry buildings during the Emilia 2012 earthquake. *Bull. Earthq. Eng.* **2014**, *12*, 2255–2273. https://doi.org/10.1007/s10518-013-9496-6.
2. D'Ayala, D.F.; Paganoni, S. Assessment and analysis of damage in L'Aquila historic city centre after 6th April 2009. *Bull. Earthq. Eng.* **2011**, *9*, 81–104. https://doi.org/10.1007/s10518-010-9224-4.
3. Sorrentino, L.; Cattari, S.; da Porto, F.; Magenes, G.; Penna, A. Seismic behaviour of ordinary masonry buildings during the 2016 central Italy earthquakes. *Bull. Earthq. Eng.* **2019**, *17*, 5583–5607. https://doi.org/10.1007/s10518-018-0370-4.
4. Stepinac, M.; Lourenço, P.B.; Atalić, J.; Kišiček, T.; Uroš, M.; Baniček, M.; Šavor Novak, M. Damage classification of residential buildings in historical downtown after the ML5.5 earthquake in Zagreb, Croatia in 2020. *Int. J. Disaster Risk Reduct.* **2021**, *56*, 102140. https://doi.org/10.1016/j.ijdrr.2021.102140.
5. Heyman, J. *The Stone Skeleton: Structural Engineering of Masonry Architecture*; Cambridge University Press: Cambridge, UK, 1995. https://doi.org/10.1017/CBO9781107050310.
6. Lourenço, P.B. Computations on historic masonry structures. *Prog. Struct. Eng. Mater.* **2002**, *4*, 301–319. https://doi.org/10.1002/pse.120.
7. Roca, P.; Cervera, M.; Gariup, G.; Pelà, L. Structural Analysis of Masonry Historical Constructions. Classical and Advanced Approaches. *Arch. Comput. Methods Eng.* **2010**, *17*, 299–325. https://doi.org/10.1007/s11831-010-9046-1.
8. Dinani, A.T.; Destro Bisol, G.; Ortega, J.; Lourenço, P.B. Structural performance of the Esfahan Shah mosque. *J. Struct. Eng.* **2021**, *147*, 05021006. https://doi.org/10.1061/(ASCE)ST.1943-541X.0003097.
9. D'Altri, A.M.; Sarhosis, V.; Milani, G.; Rots, J.; Cattari, S.; Lagomarsino, S.; Sacco, E.; Tralli, A.; Castellazzi, G.; de Miranda, S. Modeling Strategies for the Computational Analysis of Unreinforced Masonry Structures: Review and Classification. *Arch. Comput. Methods Eng.* **2020**, *27*, 1153–1185. https://doi.org/10.1007/s11831-019-09351-x.
10. Lagomarsino, S.; Penna, A.; Galasco, A.; Cattari, S. TREMURI program: An equivalent frame model for the nonlinear seismic analysis of masonry buildings. *Eng. Struct.* **2013**, *56*, 1787–1799. https://doi.org/10.1016/j.engstruct.2013.08.002.
11. Penna, A.; Lagomarsino, S.; Galasco, A. A nonlinear macroelement model for the seismic analysis of masonry buildings. *Earthq. Eng. Struct. Dyn.* **2014**, *43*, 159–179. https://doi.org/10.1002/eqe.2335.
12. Quagliarini, E.; Maracchini, G.; Clementi, F. Uses and limits of the Equivalent Frame Model on existing unreinforced masonry buildings for assessing their seismic risk: A review. *J. Build. Eng.* **2017**, *10*, 166–182. https://doi.org/10.1016/j.jobe.2017.03.004.
13. Vanin, F.; Penna, A.; Beyer, K. A three-dimensional macroelement for modelling the in-plane and out-of-plane response of masonry walls. *Earthq. Eng. Struct. Dyn.* **2020**, *49*, 1365–1387. https://doi.org/10.1002/eqe.3277.

14. Addessi, D.; Liberatore, D.; Masiani, R. Force-based beam finite element (FE) for the pushover analysis of masonry buildings. *Int. J. Archit. Herit.* **2015**, *9*, 231–243. https://doi.org/10.1080/15583058.2013.768309.
15. Siano, R.; Roca, P.; Camata, G.; Pelà, L.; Sepe, V.; Spacone, E.; Petracca, M. Numerical investigation of non-linear equivalent-frame models for regular masonry walls. *Eng. Struct.* **2018**, *173*, 512–529. https://doi.org/10.1016/j.engstruct.2018.07.006.
16. Vanin, F.; Penna, A.; Beyer, K. Equivalent-Frame Modeling of Two Shaking Table Tests of Masonry Buildings Accounting for Their Out-Of-Plane Response. *Front. Built Environ.* **2020**, *6*, 42. https://doi.org/10.3389/fbuil.2020.00042.
17. Monsef Ahmadi, H.; Zucconi, M.; Formisano, A.; Ferracuti, B. Seismic retrofitting of masonry walls using regular steel grids and steel web plates. *Procedia Struct. Integr.* **2026**, *78*, 1745–1752. https://doi.org/10.1016/j.prostr.2025.12.222.
18. Wang, C.; Sarhosis, V.; Nikitas, N. Strengthening/Retrofitting Techniques on Unreinforced Masonry Structure/Element Subjected to Seismic Loads: A Literature Review. *Open Constr. Build. Technol. J.* **2018**, *12*. https://doi.org/10.2174/1874836801812010251.
19. Napoli, A.; Realfonzo, R. FRP confined masonry under compression: Database collection and design proposals. *Compos. Struct.* **2021**, *276*, 114490. https://doi.org/10.1016/j.compstruct.2021.114490.
20. Zhuge, Y. FRP-retrofitted URM walls under in-plane shear: Review and assessment of available models. *J. Compos. Constr.* **2010**, *14*, 743–753. https://doi.org/10.1061/(ASCE)CC.1943-5614.0000135.
21. Maljaee, H.; Ghiassi, B.; Lourenço, P.B.; Oliveira, D.V. FRP-brick masonry bond degradation under hygrothermal conditions. *Compos. Struct.* **2016**, *147*, 143–154. https://doi.org/10.1016/j.compstruct.2016.03.037.
22. Ramirez, R.; Maljaee, H.; Ghiassi, B.; Lourenço, P.B.; Oliveira, D.V. Bond behavior degradation between FRP and masonry under aggressive environmental conditions. *Mech. Adv. Mater. Struct.* **2019**, *26*, 6–14. https://doi.org/10.1080/15376494.2018.1534164.
23. Shahzad, M.M.; Zhang, X.; Wang, X.; Abdulhadi, M. Comparative response assessment of different steel plate shear walls (SPSWs) under near-field ground motion. *J. Constr. Steel Res.* **2022**, *190*, 107147. https://doi.org/10.1016/j.jcsr.2022.107147.
24. Monsef Ahmadi, H.; Zucconi, M.; Ferracuti, B.; Formisano, A. *Enhancing Seismic Performance of Steel Plate Shear Walls Through Innovative Design and Curved Shape Slots*; Springer: Berlin/Heidelberg, Germany, 2024. https://doi.org/10.1007/978-3-031-62888-7_77.
25. Monsef Ahmadi, H.; Zucconi, M.; Formisano, A.; Ferracuti, B. Structural Performance and Failure Analysis of Novel Steel Plate Shear Walls. In *Proceedings of the 4th International Conference of Steel and Composite for Engineering Structures (4th ICSCES)*; Springer: Berlin/Heidelberg, Germany, 2025. https://doi.org/10.1007/978-3-032-04350-4_4.
26. Shahzad, M.M.; Zhang, X.A.; Wang, X.; Abdulhadi, M.; Wang, T.; Xiao, Y. Response control analysis of a new mega-subcontrolled structural system (MSCSS) under seismic excitation. *Struct. Des. Tall Spec. Build.* **2022**, *31*, e1935. https://doi.org/10.1002/tal.1935.
27. Wang, T.; Zhang, X.; Yang, S.; Shahzad, M.M. Quantifying the influence of modeling uncertainties on performance evaluation of mega column-core tube-outrigger structure under near-field and far-field ground motions. *J. Build. Eng.* **2022**, *59*, 105052. https://doi.org/10.1016/j.jobe.2022.105052.
28. Fan, B.; Zhang, X.; Xiao, Y.; Abdulhadi, M.; Wang, X.; Shahzad, M.M. Failure Mode and Optimization for MSCSS with LRBs Based on IDA Method. *Buildings* **2022**, *12*, 998. https://doi.org/10.3390/buildings12070998.
29. Beyer, K.; Tondelli, M.; Petry, S.; Peloso, S. Dynamic testing of a four-storey building with reinforced concrete and unreinforced masonry walls: Prediction, test results and data set. *Bull. Earthq. Eng.* **2015**, *13*, 3015–3064. https://doi.org/10.1007/s10518-015-9752-z.
30. Triantafillou, T.C. Strengthening of Masonry Structures Using Epoxy-Bonded FRP Laminates. *J. Compos. Constr.* **1998**, *2*, 96–104. https://doi.org/10.1061/(ASCE)1090-0268(1998)2:2(96).
31. Chuang, S.; Zhuge, Y.; Wong, T.; Peters, L. Seismic retrofitting of unreinforced masonry walls by FRP strips. In Proceedings of the Pacific conference on Earthquake Engineering, Christchurch, New Zealand, 13–15 February 2003.
32. ElGawady, M.A.; Asce, M.; Lestuzzi, P.; Badoux, M. Static Cyclic Response of Masonry Walls Retrofitted with Fiber-Reinforced Polymers. *J. Compos. Constr.* **2007**, *11*, 50–61. https://doi.org/10.1061/(asce)1090-0268(2007)11:1(50).
33. ElGawady, M.A.; Lestuzzi, P.; Badoux, M. Aseismic retrofitting of unreinforced masonry walls using FRP. *Compos. Part B Eng.* **2005**, *37*, 148–162. https://doi.org/10.1016/j.compositesb.2005.06.003.
34. Stratford, T.; Pascale, G.; Manfroni, O.; Bonfiglioli, B. Shear Strengthening Masonry Panels with Sheet Glass-Fiber Reinforced Polymer. *J. Compos. Constr.* **2004**. *8*, 434–443. https://doi.org/10.1061/(asce)1090-0268(2004)8:5(434).
35. Wang, Q.; Chai, Z.; Huang, Y.; Yang, Y.; Zhang, Y. Seismic shear capacity of brick masonry wall reinforced by GFRP. *Asian J. Civil Eng.* **2006**, *7*, 563–580.
36. Marcari, G.; Manfredi, G.; Prota, A.; Pecce, M. In-plane shear performance of masonry panels strengthened with FRP. *Compos. Part B Eng.* **2007**, *38*, 887–901.
37. Alcaino, P.; Santa-Maria, H. Experimental Response of Externally Retrofitted Masonry Walls Subjected to Shear Loading. *J. Compos. Constr.* **2008**, *12*, 489–498. https://doi.org/10.1061/(ASCE)1090-0268(2008)12:5(489).
38. Capozucca, R. Experimental analysis of historic masonry walls reinforced by CFRP under in-plane cyclic loading. *Compos. Struct.* **2011**, *94*, 277–289. https://doi.org/10.1016/j.compstruct.2011.06.007.

39. Zhou, D.; Lei, Z.; Wang, J. In-plane behavior of seismically damaged masonry walls repaired with external BFRP. *Compos. Struct.* **2013**, *102*, 9–19. https://doi.org/10.1016/j.compstruct.2013.01.031.
40. Triller, P.; Tomaževi, M.; Lutman, M.; Gams, M. Seismic behavior of strengthened URM masonry—An overview of research at ZAG. *Procedia Eng.* **2017**. *193*, 66–73. https://doi.org/10.1016/j.proeng.2017.06.187.
41. Hamed, E.; Rabinovitch, O. Failure characteristics of FRP-strengthened masonry walls under out-of-plane loads. *Eng. Struct.* **2010**, *32*, 2134–2145. https://doi.org/10.1016/j.engstruct.2010.03.016.
42. Anil, Ö.; Tatayolu, M.; Demirhan, M. Out-of-plane behavior of unreinforced masonry brick walls strengthened with CFRP strips. *Constr. Build. Mater.* **2012**, *35*, 614–624. https://doi.org/10.1016/j.conbuildmat.2012.04.058.
43. Willis, C.R.; Yang, Q.; Seracino, R.; Griffith, M.C. Damaged masonry walls in two-way bending retrofitted with vertical FRP strips. *Constr. Build. Mater.* **2009**, *23*, 1591–1604. https://doi.org/10.1016/j.conbuildmat.2007.09.007.
44. Tan, K.H.; Patoary, M.K.H. Strengthening of Masonry Walls against Out-of-Plane Loads Using Fiber-Reinforced Polymer Reinforcement. *J. Compos. Constr.* **2004**, *8*, 79–87.
45. Mosallam, A.S. Out-of-plane flexural behavior of unreinforced red brick walls strengthened with FRP composites. *Compos. Part B Eng.* **2007**, *38*, 559–574. https://doi.org/10.1016/j.compositesb.2006.07.019.
46. Sistani Nezhad, R.; Kabir, M.Z. Experimental investigation on out-of-plane behavior of GFRP retrofitted masonry panels. *Constr. Build. Mater.* **2017**, *131*, 630–640. https://doi.org/10.1016/j.conbuildmat.2016.11.118.
47. Gilstrap, J.M.; Dolan, C.W. Out-of-plane bending of frp-reinforced masonry walls. *Compos. Sci. Technol.* **1998**, *58*, 1277–1284. https://doi.org/10.1016/S0266-3538(98)00007-4.
48. Hamoush, S.A.; McGinley, M.W.; Mlakar, P.; Scott, D.; Murray, K. Out-of-Plane Strengthening of Masonry Walls with Reinforced Composites. *J. Compos. Constr.* **2001**, *5*, 139–145. https://doi.org/10.1061/(ASCE)1090-0268(2001)5:3(139).
49. Gattesco, N.; Amadio, C.; Bedon, C. Experimental and numerical study on the shear behavior of stone masonry walls strengthened with GFRP reinforced mortar coating and steel-cord reinforced repointing. *Eng. Struct.* **2015**, *90*, 143–157. https://doi.org/10.1016/j.engstruct.2015.02.024.
50. Scacco, J.; Ghiassi, B.; Milani, G.; Lourenço, P.B. A fast modeling approach for numerical analysis of unreinforced and FRCM reinforced masonry walls under out-of-plane loading. *Compos. Part B Eng.* **2020**, *180*, 107553. https://doi.org/10.1016/j.compositesb.2019.107553.
51. Bui, T.l.; Djamai, Z.I.; Larbi, A.S.; Reboul, N. Numerical study of composite material (FRP / TRC) -reinforced masonry walls under in-plane loading. *J. Compos. Mater.* **2021**, *55*, 3425–3441. https://doi.org/10.1177/00219983211015280.
52. Grande, E.; Imbimbo, M.; Sacco, E. A beam finite element for nonlinear analysis of masonry elements with or without fiber-reinforced plastic (FRP) reinforcements. *Int. J. Archit. Herit.* **2011**, *5*, 693–716. https://doi.org/10.1080/15583058.2010.490616.
53. Salvatori, C.; Guerrini, G.; Galasco, A.; Penna, A. Numerical Seismic Assessment of Strengthened Masonry Piers through a Novel 3D Nonlinear Macroelement. In Proceedings of the 15th Canadian Masonry Symposium, Ottawa, ON, Canada, 2–5 June 2025.
54. Caliò, I.; Marletta, M.; Pantò, B. A new discrete element model for the evaluation of the seismic behaviour of unreinforced masonry buildings. *Eng. Struct.* **2012**, *40*, 327–338. https://doi.org/10.1016/j.engstruct.2012.02.039.
55. Pantò, B.; Cannizzaro, F.; Caddemi, S.; Caliò, I.; Chácara, C.; Lourenço, P.B. Nonlinear Modelling of Curved Masonry Structures after Seismic Retrofit through FRP Reinforcing. *Buildings* **2017**, *7*, 79. https://doi.org/10.3390/buildings7030079.
56. Doherty, K.; Griffith, M.C.; Lam, N.; Wilson, J. Displacement-based seismic analysis for out-of-plane bending of unreinforced masonry walls. *Earthq. Eng. Struct. Dyn.* **2002**, *31*, 833–850. https://doi.org/10.1002/eqe.126.
57. Stepinac, M.; Hafner, I.; Stepinac, M.; Hafner, I.; Hafner, I.; Stepinac, M.; Hafner, I. Strengthening of masonry walls with FRP or TRM. *Građevinar* **2020**. *72*, 937–953.
58. *CNR-DT 200 R1/2013*; Guide for the Design and Construction of Externally Bonded FRP Systems for Strengthening Existing Structures. National Research Council: Rome, Italy, 2013.
59. Milani, G.; Grande, E.; Bertolesi, E.; Rotunno, T.; Fagone, M. Debonding mechanism of FRP strengthened flat surfaces : Analytical approach and closed form solution. *Constr. Build. Mater.* **2021**, *302*, 124144. https://doi.org/10.1016/j.conbuildmat.2021.124144.
60. Triantafillou, T.C.; Antonopoulos, C. Design of concrete flexural members strengthened in shear with FRP. *ASCE J. Mater. Civ. Eng.* **2000**, *4*, 198–205. https://doi.org/10.1061/(ASCE)1090-0268(2000)4:4(198).
61. *ACI-440.7R-10*; Guide for the Design and Construction of Externally Bonded Fiber Reinforced Polymer Systems for Strengthening Unreinforced Masonry Structures. American Concrete Institute: Farmington Hills, MI, USA, 2010.
62. *EN 1998-1:2004*; Eurocode 8: Design of Structures for Earthquake Resistance—Part 1: General Rules, Seismic Actions and Rules for Buildings. Technical report. https://eurocodes.jrc.ec.europa.eu/EN-Eurocodes/eurocode-8-design-structures-earthquake-resistance. European Committee for Standardization (CEN): Brussels, Belgium, 2004.
63. Prota, A.; Manfredi, G.; Nardone, F. Assessment of Design Formulas for In-Plane FRP Strengthening of Masonry Walls. *J. Compos. Constr.* **2008**, *12*, 643–649. https://doi.org/10.1061/(ASCE)1090-0268(2008)12:6(643).
64. McKenna, F.; Fenves, G.; Scott, M.; Jeremic, B. *Open System for Earthquake Engineering Simulation (OpenSees)*; University of California: Berkeley, CA, USA. 2000. Available online: http://opensees.berkeley.edu (accessed on 20 February 2020)

65. Wilding, B.V.; Godio, M.; Beyer, K. The ratio of shear to elastic modulus of in-plane loaded masonry. *Mater. Struct.* **2020**, *53*, 40. https://doi.org/10.1617/s11527-020-01464-1.
66. Kržan, M.; Gostič, S.; Cattari, S.; Bosiljkov, V. Acquiring reference parameters of masonry for the structural performance analysis of historical buildings. *Bull. Earthq. Eng.* **2015**, *13*, 203–236. https://doi.org/10.1007/s10518-014-9686-x.
67. ElGawady, M. Seismic In-Plane Behavior of URM Walls Upgraded with Composites. Ph.D. Thesis, EPFL, Lausanne, Switzerland, 2004. https://doi.org/10.5075/epfl-thesis-3111.
68. Marcari, G.; Fabbrocino, G.; Manfredi, G.; Prota, A. Experimental and numerical evaluation of tuff masonry panels shear seismic capacity. In *Proceedings of the 10th North American Masonry Conference*; The Masonry Society: Fort Collins, CO, USA, 2007.
69. Vanin, F.; Zaganelli, D.; Penna, A.; Beyer, K. Estimates for the stiffness, strength and drift capacity of stone masonry walls based on 123 quasi-static cyclic tests reported in the literature. *Bull. Earthq. Eng.* **2017**, *15*, 5435–5479. https://doi.org/10.1007/s10518-017-0188-5.
70. Tomaževič, M. Shear resistance of masonry walls and Eurocode 6: Shear versus tensile strength of masonry. *Mater. Struct./Mater. Et Constr.* **2009**, *42*, 889–907. https://doi.org/10.1617/s11527-008-9430-6.
71. Saleem, M.U.; Numada, M.; Amin, M.N.; Meguro, K. Seismic response of PP-band and FRP retrofitted house models under shake table testing. *Constr. Build. Mater.* **2016**, *111*, 298–316. https://doi.org/10.1016/j.conbuildmat.2016.02.073.
72. Krstevska, L.; Shendova, V.; Rakicevic, Z.T.; Tashkov, L. Shaking Table Testing of Models of Historic Buildings and Monuments-IZIIS ' Experience. In *Role of Seismic Testing Facilities in Performance-Based Earthquake Engineering: SERIES Workshop*; Springer: Dordrecht, The Netherlands, 2010. https://doi.org/10.1007/978-94-007-1977-4.
73. Gu, J.B.; Tao, Y.; Xin, R.; Yang, Z.; Shi, Q.X. Seismic Performance of Multistorey Masonry Structure with Openings Repaired with CFRP Grid. *Adv. Civ. Eng.* **2018**, *2018*, 4374876. https://doi.org/10.1155/2018/4374876.
74. Triller, P.; Tomaževič, M.; Gams, M. Seismic strengthening of clay block masonry buildings with composites: An experimental study of a full scale three-storey building model. *Bull. Earthq. Eng.* **2019**, *17*, 4049–4080. https://doi.org/10.1007/s10518-019-00609-0.
75. Tondelli, M.; Beyer, K.; DeJong, M. Influence of boundary conditions on the out-of-plane response of brick masonry walls in buildings with RC slabs. *Earthq. Eng. Struct. Dyn.* **2016**, *45*, 1337–1356. https://doi.org/10.1002/eqe.2710.
76. Paparoa, A.; Beyer, K. Development of a displacement-based design approach for modern mixed RC-URM wall structures. *Earthq. Struct.* **2015**, *9*, 789–830. https://doi.org/10.12989/eas.2015.9.4.789.
77. Vanin, F.; Beyer, K. Equivalent damping ratio for a macroelement modelling the out-of-plane response of masonry walls. *Earthq. Eng. Struct. Dyn. submitted*.
78. Vaculik, J.; Visintin, P.; Burton, N.G.; Griffith, M.C.; Seracino, R. State-of-the-art review and future research directions for FRP-to-masonry bond research: Test methods and techniques for extraction of bond-slip behaviour. *Constr. Build. Mater.* **2018**, *183*, 325–345. https://doi.org/10.1016/j.conbuildmat.2018.06.103.
79. *CNR-DT 215/2018*; Istruzioni per la Progettazione, l'Esecuzione ed il Controllo di Interventi di Consolidamento Statico mediante l'utilizzo di Compositi Fibrorinforzati a Matrice Inorganica. CNR, Consiglio Nazionale delle Ricerche: Rome, Italy, 2018.
80. Oddo, M.C.; Minafò, G.; La Mendola, L. Constitutive Models for the Tensile Behaviour of TRM Materials: Literature Review and Experimental Verification. *Materials* **2021**, *14*, 700. https://doi.org/10.3390/ma14030700.
81. Arboleda, D.; Carozzi, F.G.; Nanni, A.; Poggi, C. Testing Procedures for the Uniaxial Tensile Characterization of Fabric-Reinforced Cementitious Matrix Composites. *J. Compos. Constr.* **2016**, *20*, 04015063. https://doi.org/10.1061/(ASCE)CC.1943-5614.0000626.
82. Papanicolaou, C.G.; Triantafillou, T.C.; Karlos, K.; Papathanasiou, M. Textile-reinforced mortar (TRM) versus FRP as strengthening material of URM walls: In-plane cyclic loading. *Mater. Struct./Mater. Et Constr.* **2007**, *40*, 1081–1097. https://doi.org/10.1617/s11527-006-9207-8.

Disclaimer/Publisher's Note: The statements, opinions and data contained in all publications are solely those of the individual author(s) and contributor(s) and not of MDPI and/or the editor(s). MDPI and/or the editor(s) disclaim responsibility for any injury to people or property resulting from any ideas, methods, instructions or products referred to in the content.